Hergenrother Carl, W (Orcid ID: 0000-0002-9120-7212)

Chesley Steven (Orcid ID: 0000-0003-3240-6497)

French Andrew (Orcid ID: 0000-0002-3427-1920)

Davis Alex, B. (Orcid ID: 0000-0003-2082-5176)

Pelgrift John, Y (Orcid ID: 0000-0003-4574-8795)

Leonard Jason, M (Orcid ID: 0000-0003-3632-6793)

Liounis Andrew (Orcid ID: 0000-0001-8867-5253)

Becker Kris, J (Orcid ID: 0000-0003-1971-5957)

Adam Coralie, D (Orcid ID: 0000-0002-5795-2446)

Burke Keara (Orcid ID: 0000-0003-1633-2096)

Clark Beth Ellen (Orcid ID: 0000-0002-2407-2880)

Farnocchia Davide (Orcid ID: 0000-0003-0774-884X)

Lessac-Chenen Erik (Orcid ID: 0000-0001-7015-9111)

Nolan Michael, C (Orcid ID: 0000-0001-8316-0680)

Park Ryan S. (Orcid ID: 0000-0001-9896-4585)

Selznick Sanford (Orcid ID: 0000-0002-3182-6783)

Rizk Bashar (Orcid ID: 0000-0002-0823-9804)

Photometry of particles ejected from active asteroid (101955) Bennu

C. W. Hergenrother[1], C. Maleszewski[1], J.-Y. Li[2], M. Pajola[3], S. R. Chesley[4], A. S. French[4], A. B. Davis[5], J. Y. Pelgrift[6], J. M. Leonard[6], F. Shelly[1], A. J. Liounis[7], K. Becker[1], S. S. Balram-Knutson[1], R. Garcia[1], T. R. Kareta[1], C. Adam[6], K. Alkiek[7], B. J. Bos[7], M. Brozović[4], K. N. Burke[1], E. Christensen[1], B. E. Clark[8], D. N. DellaGiustina[1], C. Drouet d'Aubigny[1], D. Farnocchia[4], E. S. Howell[1], R. A. Jacobson[4], J. N. Kidd[1], E. J. Lessac-Chenen[6], R. Melikyan[8], M. C. Nolan[1], R. S. Park[4], S. Selznick[1], B. Rizk[1], D. S. Lauretta[1]

[1]Lunar and Planetary Laboratory, University of Arizona, Tucson, USA.

[2]Planetary Science Institute, Tucson, Arizona, USA.

[3]INAF - Astronomical Observatory of Padova, Padova, Italy.

[4]Jet Propulsion Laboratory, California Institute of Technology, Pasadena, California, USA.

[5]Department of Aerospace Engineering Sciences, University of Colorado-Boulder, Boulder, Colorado, USA.

[6]KinetX Aerospace, Simi Valley, California, USA.

[7]Goddard Space Flight Center, Greenbelt, Maryland, USA.

[8]Department of Physics and Astronomy, Ithaca College, Ithaca New York, USA,

Corresponding author: Carl Hergenrother (chergen@lpl.arizona.edu)

Key Points:

- Asteroid (101955) Bennu is active from perihelion through aphelion with a possible decrease in activity further from the Sun

- Bennu's activity is less than that detected by telescope for other active asteroids and is only observable up close

- The particles' shallow phase functions resemble those of similarly sized individual rocks rather than those of ensemble asteroid surfaces

Abstract

Near-Earth asteroid (101955) Bennu is an active asteroid experiencing mass loss in the form of ejection events emitting up to hundreds of millimeter- to centimeter-scale particles. The close proximity of the Origins, Spectral Interpretations, Resource Identification, and Security–Regolith Explorer (OSIRIS-REx) spacecraft enabled monitoring of particles for a 10-month period encompassing Bennu's perihelion and aphelion. We found eighteen multi-particle ejection events, with masses ranging from near zero to hundreds of grams (or thousands with uncertainties) and translational kinetic energies ranging from near zero to tens of millijoules (or hundreds with uncertainties). We estimate that Bennu ejects ~10^4 g per orbit. The largest event took place on 6 January 2019 and consisted of ~200 particles. The observed mass and translational kinetic energy of the event were between 459 and 528 g and 62 and 77 mJ, respectively. Hundreds of particles not associated with the multi-particle ejections were also observed. Photometry of the best-observed particles, measured at phase angles between ~70° and 120°, was used to derive a linear phase coefficient of 0.013 ± 0.005 magnitudes per degree of phase angle. Ground-based data back to 1999 show no evidence of past activity for Bennu, however, the currently observed activity is orders of magnitude lower that that observed at other active asteroids and too low be observed remotely. There appears to be a gentle decrease in activity with distance from the Sun, suggestive of ejection processes such as meteoroid impacts and thermal fracturing, although observational bias may be a factor.

Plain Language Summary

We measured the brightness of pebble-sized particles in the vicinity of near-Earth asteroid Bennu to better understand their physical characteristics and the events that launched them from Bennu's surface. Our measurements spanned 10 months, encompassing Bennu's closest and farthest distances from the Sun, so that we could assess how the level of ejection activity changes with solar distance. We observed 18 multi-particle ejection events containing anywhere from a few to 200+ particles. Individual particles ranged from millimeters to centimeters in diameter. The energy of the events and a possible decrease in activity with larger distances from the Sun suggest that meteoroid impacts, fracturing of surface boulders due to solar heating, or both may be responsible for ejecting the particles. We estimate that Bennu releases ~10,000 g of material over one orbit, or 1.2 years. Although mass loss has been remotely observed for other asteroids, the comparatively low level of particle ejection activity at Bennu was only observable thanks to the close proximity of the OSIRIS-REx spacecraft.

1. Introduction

Active asteroids are small solar system objects, with origins in the Main Belt, exhibiting mass loss [*Jewitt et al.,* 2015]. An early finding of the Origins, Spectral Interpretations, Resource Identification, and Security–Regolith Explorer (OSIRIS-REx) mission was the observation of mass loss from near-Earth asteroid (101955) Bennu manifesting as a population of millimeter- to centimeter-scale particles ejected from the asteroid surface [*Hergenrother et al.,* 2019; *Lauretta et al.,* 2019; *Lauretta & Hergenrother et al.,* 2019]. This observed mass loss, combined with Bennu's origin in the inner Main Belt

[*Campins et al.,* 2010], makes Bennu an active asteroid [*Jewitt et al.,* 2015]. Bennu now joins (1) Ceres as the only active asteroids to be studied by spacecraft in close proximity [*Küppers et al.,* 2014].

The active asteroid classification is a catchall category without regard for the responsible mechanism. The lack of certainty about how mass is lost is due to active asteroids being remotely observed by ground-based or near-Earth telescopes. Such observations are limited to photometric, morphological, and orbital analysis. *Lauretta and Hergenrother et al.* [2019] considered seven candidate mechanisms for the ejection events at Bennu, including rotational disruption, electrostatic lofting, ice sublimation, phyllosilicate dehydration, thermal stress fracturing, meteoroid impacts, and secondary surface impacts by returning Bennu particles. Phyllosilicate dehydration, thermal stress fracturing, and meteoroid impacts were found to be the most plausible mechanisms for the largest observed events, with secondary impacts possible for smaller events. More detailed evaluation of candidate mechanisms can be found in *Hartzell et al.* [in review, this collection] for electrostatic lofting, *Bottke et al.* [in review, this collection] for meteoroid impacts, *Rozitis et al.* [accepted, this collection] for ice sublimation, and *Molaro et al.* [in review, this collection] and *Rozitis et al.* [accepted, this collection] for thermal fracturing. An example of a particle ejected by means of a secondary surface impact was identified by *Chesley et al.* [in review, this collection].

Bennu was selected as the target of OSIRIS-REx primarily due to its presumed carbonaceous composition, accessible orbit for sample return, and extensive physical characterization [*Lauretta et al.,* 2015]. The B-type taxonomy of Bennu links it to active asteroids experiencing volatile sublimation [*Campins et al.,* in review, this collection]. Examples of B-type active bodies include Main Belt objects 133P/Elst-Pizarro and 176P/LINEAR [Licandro et al., 2011] and near-Earth objects (3200) Phaethon, 107P/Wilson-Harrington, and 249P/LINEAR [Fernández et al., 2017]. 107P/Wilson-Harrington and 249P/LINEAR have a dynamical history suggestive of an origin in the Main Belt and may be active asteroids perturbed into the near-Earth population [Fernández and Sosa, 2015; Fernández et al., 2017]. Phaethon is the parent body of the major annual Geminid meteor shower [*Whipple,* 1983] and has been observed to experience mass loss near perihelion [*Jewitt and Li,* 2010].

The millimeter- to centimeter-scale particles at Bennu are among the smallest discrete natural bodies observed above Earth's atmosphere. Large gravitationally bound cometary grains detected around comets 67P/Churyumov-Gerasimenko and 103P/Hartley are the closest match in terms of discrete particle size [*Hermalyn et al.,* 2013; *Davidsson et al.,* 2015; *Levasseur-Regourd et al.,* 2018]. However, these cometary particles can be larger than the Bennu particles with diameters of decimeters to meters.

In this paper, we present photometry of particles ejected from Bennu, spanning the detection of the first known particle in December 2018 through the end of dedicated particle monitoring in September 2019. This time range covers the outbound journey of Bennu from perihelion to aphelion. Section 2 presents the methods used to detect particles in OSIRIS-REx image data and perform point spread function (PSF) fitting photometry. Section 3 describes the OSIRIS-REx mission phases and the particle observations conducted during each. In Section 4, we present our results including an analysis of the photometric and bulk properties of individual particles, as well as the bulk properties of the ensemble population and the ejection events, and we investigate whether Bennu's activity could be observed by remote

telescopes. The results presented here provide a physical basis for analysis and interpretation of the particle ejection phenomenon over the full range of Bennu-Sun distances. They further contextualize the observed activity at Bennu with respect to the broader population of active asteroids, shedding light on the continuum of asteroid activity in the solar system.

2. Methods

The primary instrument for particle detection was the NavCam 1 camera, which is part of the OSIRIS-REx Touch And Go Camera System (TAGCAMS) [*Bos et al.,* 2018; *Bos et al.,* submitted]. As the name suggests, this camera was intended for optical navigation (OpNav) rather than scientific observation. However, dedicated science observations during the spacecraft's approach to the asteroid failed to detect activity (*Hergenrother et al.,* 2019; discussed further in section 3), whereas NavCam 1's large field of view (FOV) and daily imaging of the region around Bennu allowed it to serendipitously detect ejected particles once the spacecraft was in close proximity to Bennu. The NavCam 1 detector is an ON Semiconductor (formerly Aptina) MT9P031 5-megapixel image sensor with an active focal plane of 2592 × 1944, 2.2-micron pixels and on-chip 12-bit digitization. The optical assembly consists of a seven-element all-refractive lens with an aperture diameter of 2.2 mm and a nominal focal length of 7.6 mm. The system produces a FOV of about 44° × 32° and an on-axis pixel scale of 288 μrad per pixel, or roughly 58 arc seconds per pixel. NavCam 1 is a panchromatic camera with a broadband response between ~400-700 nm.

Particles were seen as groups of up to hundreds of particles radiating from a common source region on the surface of Bennu (ejection events), or as single particles in near-Bennu space. Different particle detection methods were used depending on whether we were searching for large ejection events or single particles. Individual particle detections were identified in the NavCam 1 images and reported in both detector XY coordinates and celestial coordinates (right ascension and declination). Sequences of detections attributable to individual particles were designated as tracks. Orbit determination (OD) of tracks produced orbital solutions [*Lauretta and Hergenrother et al.,* 2019; *Chesley et al.,* in review, this collection; *Leonard et al.,* accepted, Earth and Space Science, this collection; *Pelgrift et al.,* accepted, Earth and Space Science, this collection]. Some particles that remained in the Bennu environment for an extended period (days) were observed in multiple tracks. In those cases, individual tracks were linked together.

2.1. Moving Object Detection

2.1.1. Visual inspection

The most basic form of particle detection is the visual identification of moving objects based on their motion relative to fixed background stars, colloquially known as blinking images. In most NavCam 1 images, Bennu is also in the FOV. The visibility of particles in visually inspected images was enhanced by minimizing non-uniform in-field stray light from Bennu through the production of a Gaussian convolved image. This technique is a variant of the classical unsharp masking and commonly used to enhance the visibility of fine features within the comae of comets [*Samarasinha & Larson,* 2014]. Visual blinking of images was used for first-look inspections and when the imaging cadence was not optimal for automated software detection, i.e., time between pairs is large so particles are only visible in one or two images. It proved a quick and efficient way to detect large ejection events.

A second manual technique that we used was the visual inspection of an image created by the division of one image by the other image in a pair taken close together in time. Moving objects in a differenced image appear as positive-negative sets of sources. This and the aforementioned technique were often used in combination where a series of differenced images are blinked. The manual techniques were time-intensive and affected by the time-dependent experience and sensitivity of the human inspector. Due to these limitations, the development of automated detection solutions was pursued.

2.1.2. Automated detection software

Two software suites were modified to detect particles with varying levels of manual intervention. The Goddard Image Analysis and Navigation Tool (GIANT) was originally developed to help analyze optical navigation (OpNav) images [*Liounis et al.* in review, this collection]. New algorithms were implemented to extract observations of potential particles from the images and generate linkages between potential detections of the same particle. GIANT was utilized within weeks of the first recognized particles. GIANT identified all point sources in an image and flagged those not corresponding to catalog stars. The extraneous sources were overlaid on an image, allowing quick manual inspection for particles. The process was further streamlined by the production of visual aids in the form of plots for each image showing the location of extraneous sources in each FOV (see Figures 7 to 10 in *Liounis et al.* [in review]). When the second algorithm was implemented, automatic linked tracks were also displayed in the plots.

The other automated approach is a modification of the moving object detection pipeline developed by the Catalina Sky Survey (CSS) [*Christensen et al.,* 2018]. The USGS ISIS3 (Integrated Software for Imagers and Spectrometers) system was used to produce geometric distortion–corrected images for the CSS pipeline. The pipeline search algorithms were conducted on two sequential undistorted image pairs, consisting of four images at a time. The pipeline corrected for stray light from Bennu and produced a flat background to within 15 pixels from the edge of the saturated asteroid.

The SExtractor source extraction program was used to catalog sources in the image [*Bertin and Arnouts,* 1996]. The pipeline identified GAIA-DR2 stars brighter than magnitude 7.0 that might appear in the FOV. An astrometric solution for the image using the star catalog and point sources was computed with the SCAMP program [*Bertin,* 2010]. For the distortion corrected images, a simple 2-degree polynomial was used to calculate a fine offset and scaling and rotation parameters from the images. J2000 coordinates were calculated for each point source using the SCAMP solution. The XY positions of the identified GAIA-DR2 catalog stars were created using the WCSTOOLS program sky2xy [*Mink,* 1997]. The median offset in the magnitudes between the matched identified stars was then computed. This offset was applied to the sources not identified as stars.

Files containing point sources were produced for each of the four images with sources identified as stars removed. A density filter was used to thin out any dense clusters of point sources. The remaining point sources were run through a linkage algorithm to find four detections that moved within tune-able velocity and acceleration parameters. While two images could be used to identify moving objects, using only two images produces a large number of false positive identifications. Potential particle detections were then presented with SAOImage ds9 [*Mink,* 1997] for manual validation to determine which detections were real.

Because the pipeline searches for detections within a set of four images, it gives the observer multiple opportunities to identify particles visible in more than four images. This greatly increases the detection efficiency for long observable particles. Lastly, overlapping validated detections were linked together so that detections over four or more images can be combined into longer tracks. A limitation of the automated detection capability of the pipeline is its inability to identify a particle visible in less than four separate images, including fast moving objects that rapidly exit the image FOV.

A second manual validation step was conducted by blinking images outside of the pipeline to confirm the reality of the object. At this stage, the manual inspector could lengthen the pipeline detected tracks by finding valid detections extending the track endpoints. All CSS pipeline detections were then linked with their corresponding GIANT detection to produce tracks.

2.2. PSF photometry

We measured the total flux of particles using a PSF fitting method. In this approach, each identified source is fitted to an analytic PSF model, and the total flux of a source is calculated from the best-fit model and corrected with a pre-derived correction factor that accounts for the slightly different shape of the actual PSF and the analytic model. The steps for this approach, detailed below, are: (1) characterizing the PSF to derive an analytic PSF model and the correction factor; (2) fitting all sources to the PSF model iteratively; (3) calculating total fluxes from best-fit models and applying correction factors.

We selected PSF fitting photometry for this work instead of the aperture photometry used in *Lauretta and Hergenrother et al.* [2019] because of its improved handling of crowded sources and streaked fast-moving objects [*Stetson,* 1987; *Veres et al.,* 2012]. As a result, some values for events characterized in that study have decreased in this work (Section 4).

2.2.1. PSF model and characterization

The characteristics of the NavCam 1 PSF are described in *Bos et al.* [submitted]. Owing to the large FOV (44° x 32°) of NavCam 1 and geometric distortion, the shape and size of the PSF vary across the detector (Fig. 1). Therefore, we used PSFs extracted from 45 locations in a 9x5 grid in the NavCam 1 FOV and oversampled by a factor of 8, aligned and stacked, to derive an average PSF (Fig. 1). Then we fitted the average PSF to a 2-D circular Gaussian function and derived a full width at half maximum (FWHM) of 1.73 pixels. This is the basis of our PSF fitting. The reason that we chose a Gaussian PSF rather than other possible functional forms such as the Moffat function (*Moffat,* 1969) is because the Gaussian function allows us to easily derive an analytic model to fit streaked particles, as we discuss later.

The spatial variation of the PSF also means that the correction factor for the best-fit analytic PSF model depends on the particular locations of sources in an image. We fitted the Gaussian PSF model with the width fixed at the derived width to all 45 individual PSFs and compared the total flux contained in each best-fit model with that in the corresponding PSF to derive the correction factors for all PSFs. Fig. 2 shows the distribution of correction factors. For sources at arbitrary locations in the field, we use a bi-cubic spline interpolation to calculate the correction factors based on the 9x5 grid of correction factors that we derived.

One complication in fitting a PSF to our sources is the streaking of some particles, with some streaks more than 10 pixels long. To account for streaking, we assumed that the streaks are straight lines and convolved the 2-D circular Gaussian function with a line segment function. The derived functional form for the streaked PSF $f(x, y)$ is,

$$\frac{\mathrm{erf}\left(\frac{\left(\frac{s}{2} - y_n\right)}{\sqrt{2}\sigma}\right) + \mathrm{erf}\left(\frac{\left(\frac{s}{2} + y_n\right)}{\sqrt{2}\sigma}\right)}{2\,\mathrm{erf}\left(\frac{s}{2\sqrt{2}\sigma}\right)}$$

$$x_n = dx\cos\theta + dy\sin\theta$$
$$y_n = -dx\sin\theta + dy\cos\theta$$
$$dx = x - x_0$$
$$dy = y - y_0$$

where erf is the Gaussian error function. This model contains six model parameters: the amplitude A, the standard deviation σ of the Gaussian, the full length s of streaking, the position angle θ (counterclockwise from up direction) of the streaking, and the center of the source (x_0, y_0). When streaking $s = 0$, this model becomes a 2-D circular Gaussian function. The total flux included in this PSF model is,

$$F = \frac{\sqrt{2\pi}A\sigma s}{\mathrm{erf}\left(\frac{s}{2\sqrt{2}\sigma}\right)}$$
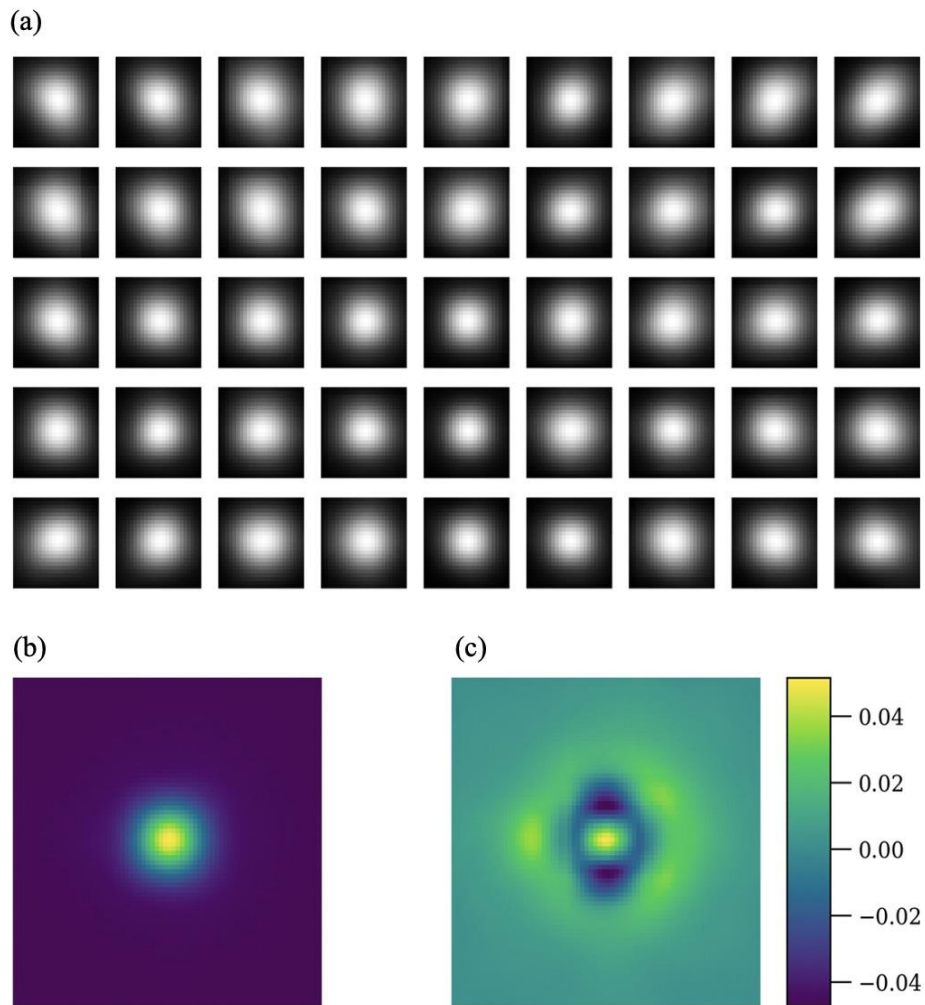
(a)

(b)

(c)

Fig. 1. (a) Composite PSFs of NavCam 1 in the 9x5 grid locations in the FOV, each PSF being oversampled by a factor of 8. (b) Average PSF generated by aligning and stacking all 45 PSFs. (c) Deviation of average PSF from the best-fit 2D circular Gaussian model. (a) and (b) are displayed in logarithmic brightness stretch. (c) is displayed in linear brightness stretch with the peak of PSF normalized to unity. The average PSF is close to round shape, with sharper peak in the center than a Gaussian and more extended wings on the outskirt.
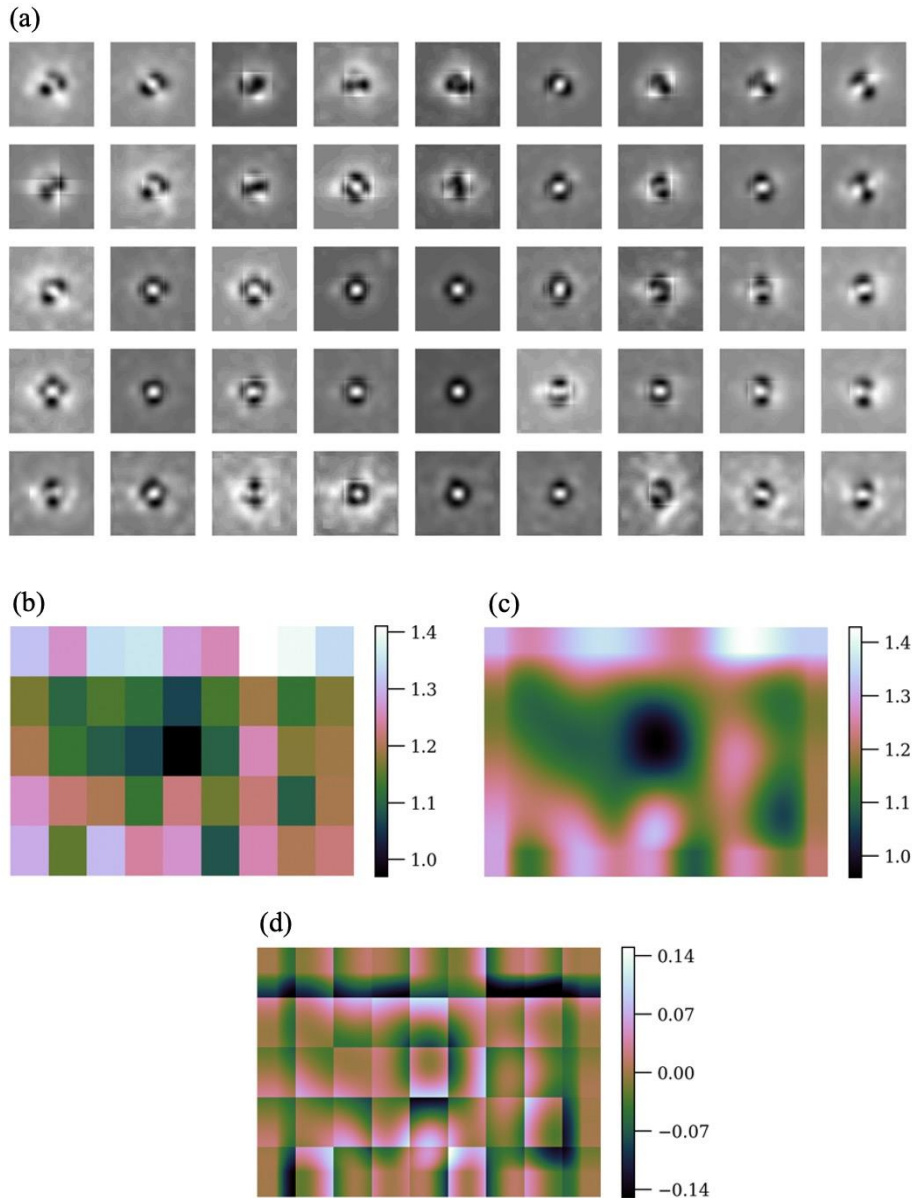
(a)

(b)

(c)

(d)

Fig. 2. (a) Deviation maps of actual PSFs and the respective best-fit PSF model with a fixed standard deviation of 0.733 pixel. (b) Correction factor map to correct for the total flux calculated from best-fit model to actual flux. (c) Correction factor map smoothed with a bi-cubic spline interpolation. (d) Difference between the smoothed correction factor map and the original correction factor map.

2.2.2. Sky background

All images with particles identified contain non-uniform in-field stray light that substantially affects photometric measurement of particles. The background has a strong gradient from about 4000 CCD digital numbers (DN) near the edge of the saturated Bennu's disk to the detector bias of between 100 and 200 DNs, and contains ghost images of Bennu. The strong gradient and the complicated structure that depends on the location of Bennu in the field make it difficult to remove the background with simple median filtering. We experimented with two approaches to treat the background.

The first approach was to build a background image iteratively and subtract it out from the original image to derive a clean image. We subtracted a moving boxcar median–filtered image from the original image first, then fit PSFs to all particles, and subtracted out the best-fit models for all particles from the original image. Then we used the source-subtracted images to construct a median-filtered image as the background image and repeated the above process to produce an improved version of the source-subtracted image. After three iterations, the background image was clean of artifacts near the sources. This background image was then subtracted from the original image to produce a background-cleaned image for photometric measurements. While this method produces a clean background near each individual particle, it still contains some artifacts in the area with strong gradient in the background, especially near Bennu.

The second approach was to include the background in the analytic PSF model when fitting the sources. We added a simple linear background model $B(x, y)$ to the PSF model described above,

$$B(x, y) = ax + by + c$$

where a, b, c are three parameters to approximate the local background in the small windows for the sources to be fitted. Experiments demonstrated that a linear background model sufficiently describes the local background and substantially improves PSF fitting. Compared to the background-removal approach, this background-fitting approach is better for the regions with the strongest gradient, such as for those particles that are close to the limb of Bennu, as well as regions with crowded sources. However, it adds three additional parameters to the model to be fitted, although the background model can usually be fitted well because all pixels inside a window can be used to fit these parameters.

We verified that the resultant total flux measurements from these two approaches agree with each other within a few percent for bright particles, and within ±10% for moderately bright particles, although in some cases of faint particles, the discrepancy can be >±50%. The second approach, including the background in the PSF model, was used for our particle photometry.

2.2.3. PSF fitting

We started by batch-fitting the analytic PSF model to all sources in an image from the brightest particle to the faintest with an automated process. The total fluxes were originally measured with aperture photometry by either the IRAF (Image Reduction and Analysis Facility) DIGIPHOT tool or GIANT [*Lauretta and Hergenrother et al.*, 2019]. The aperture photometry was used to sort the particles in the inverse order of brightness. Each particle was fitted using all the unsaturated pixels within a box of 21 x 21 pixels. This box size was chosen because it encloses the majority of streaked pixels, and the changes in the background inside the box are not severe and can be approximated by a linear function. The width parameter σ was held fixed at the value derived from the average PSF (Section 1.1), while the other eight parameters (five PSF parameters and three background parameters) were fitted. After fitting each particle, we subtracted it from the original image and fit the next brightest one. Once all the particles were fit, we used the fitted fluxes to sort the particles in the inverse order of brightness again and the fitted centroid to adjust the box locations for all particles.

Then we fit all particles for the second time. This iterative process helps fit faint sources close to bright ones.
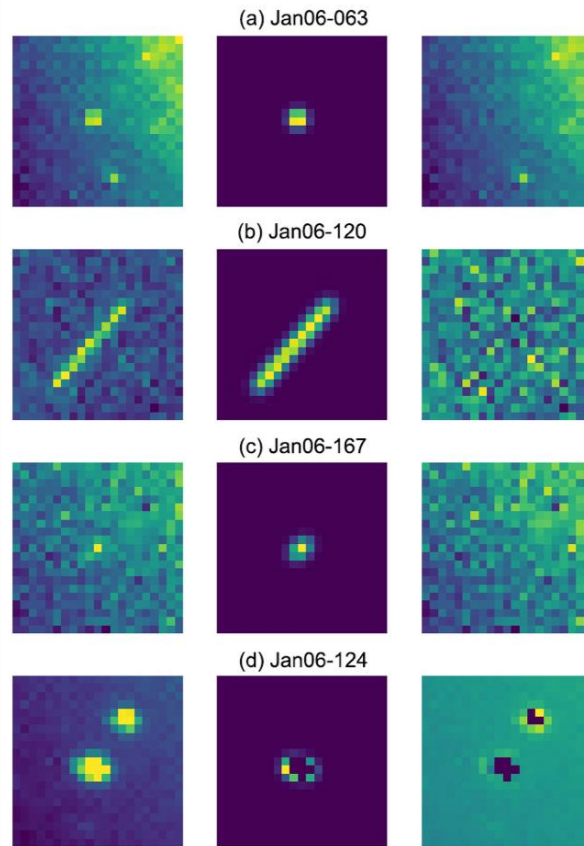

Fig. 3. Examples of successful PSF fitting for various cases. In each panel, the left column is the image snippet of 21x21 pixels in size, containing the particle to be fitted, the middle panel is the best-fit model, and the right panel is the residual. Label name corresponds to the particle ID. (a) A moderately bright particle with a strongly non-uniform background. (b) A streaked particle. (c) A faint particle just above the background and noise floor. (d) A very bright particle with the center pixels saturated (black in the middle and right columns.

Our PSF fitting process works well for the majority of particles, including streaked particles, particles with a strongly graded background, particles close to each other, and even a few particles with a saturated core (Fig. 3). For about 10% of all detections, the fit fails. The failure is due primarily to the faintness of particles that do not have enough pixels above the local noise floor to reliably derive the streaking length parameter. For those particles, we limited the streaking length parameter based on the amplitude and background. If the fitted amplitude was less than $3\times$ the local noise floor, which is estimated as photon noise from background and particle, we set the streaking to be the maximum streaking parameter of all bright particles (usually three to eight pixels). If the amplitude was less than $2\times$ the local noise, then the streaking parameter was limited to <1 pixel. And if the amplitude was less than the local noise, then the streaking parameter was set to 0.

After the batch fitting, for six ejection events on 6 January, 19 January, 11 February, 19 April, 18 June, and 13 September 2019, we inspected the snippet image in the fitting window for each source and the corresponding model residual to check for model quality. We

then manually fit every possibly problematic fit with the initial model parameters, adjusted to improve the fit until a reasonable fit was achieved. When needed, we also adjusted the size of the fitting window to accommodate the streaked particles. For less than 10 particles, we needed to decrease the box size progressively, with the streaking parameter set to 0, until the fit was successful. This final manual adjustment step applied to about 15% of all detections in these six events. We did not apply the manual fix to those particle detections from the Chesley et al. [in review, this collection] catalog. Finally, for all the particles with the best-fit streaking parameter s found to be 0 (non-streaked), we replaced the PSF model by a circular Gaussian and fit the model again.

2.2.4. Magnitude Conversion

Total DN counts measured within the fitted PSF were converted to V-band apparent magnitude m_V via

$$m_v = \left(\frac{1}{\alpha}\right) \times log10\left(\frac{DN}{t} \times \frac{1.25}{(g \times c)}\right)$$

where, for NavCam 1, $\alpha = -0.40362$, $c = 31564.2$, g is the commanded gain (1.25), DN is the total DN from the PSF fitting, t is exposure time in seconds (5 or 10 seconds), and log10 stands for the base 10 logarithm [*Lauretta and Hergenrother et al.*, 2019; *Bos et al.*, submitted].

The point source responsivity calibration which produced the DN-to-V magnitude relationship is described in *Bos et al.* [submitted]. Photometry of 1,847 stars is compared with V-band magnitudes from the U.S. Naval Observatory CCD Astrograph Catalog (UCAC4) star catalog [*Zacharias et al.*, 2013]. Magnitudes were not corrected for the difference between the colors of the stars and the broadband panchromatic response of NavCam 1. The instrument detector also has a fill factor of less than 1. The NavCam 1 photometry of the UCAC4 stars found a 1-sigma variation of ~6.4% due to the uncorrected stellar color terms and detector fill factor. A systematic error on order of ~6% is small compared to the uncertainty in the phase coefficient for the determination of absolute magnitude, and the uncertainty in albedo for the determination of particle size.

2.2.5. Uncertainty Estimate

The uncertainty estimate for our measured flux from the PSF fitting follows the standard error propagation theory using the covariance matrix of the best-fit parameters. In particular, the standard deviation of the modeled flux, σ_F, is,

$$\sigma_F^2 = \left(\frac{\partial F}{\partial A}, \frac{\partial F}{\partial \sigma}, \frac{\partial F}{\partial s}\right) (covariance) \begin{pmatrix} \frac{\partial F}{\partial A} \\ \frac{\partial F}{\partial \sigma} \\ \frac{\partial F}{\partial s} \end{pmatrix}$$

where (A, σ, s) are the amplitude, standard deviation, and streaking length of the PSF model as discussed above, that determines the modeled total flux F. The partial derivatives can be derived from the equation of total flux. The fitting algorithm returns a covariance matrix for the best-fit parameters. Because we hold the standard deviation of the PSF model constant in our fitting, the error propagation does not need to include the partial derivative with respect to σ, and the covariance matrix we used above is a 2x2 matrix. However, for some cases the fitting routine is not able to return a covariance matrix to support this approach. We are able to estimate the errors for about 90% of all the particles for which we measured the photometry. For the remainder, the error was determined to be the average error of particles of a similar brightness.

The model flux uncertainty estimated above needs to be combined with the uncertainty introduced by local background. We used the average background inside the fitting window, represented by parameter c to estimate the photon noise, and quadratically combined it with the model flux uncertainty described above to derive the total uncertainty for our total flux measurement. The overall measurement errors depend on the apparent magnitude of the particles. However, these error estimates are statistical errors due to model fitting to noisy data. Another source of error, which is systematic in nature, could potentially be introduced by the sharper center core of the actual PSF than the model PSF (Fig. 1). For faint particles, the model PSF is dominated by the center pixels that have signal levels above the local background noise. In this case, the model PSF tends to have higher best-fit amplitude parameter than the actual height, causing up to a 5% overestimate of the total flux for faint particles. In addition, the location-dependent PSF correction factor could also introduce errors of up to 15% (Fig. 2). We did not include the error introduced by the spatially varying PSF in the final uncertainties of PSF photometry because this is an upper limit uncertainty estimate that only applies to the worst case.

3. Observations

The OSIRIS-REx encounter at Bennu is divided into several mission phases: Approach, Preliminary Survey, Orbital A, Detailed Survey, Orbital B, Orbital C, Reconnaissance, Rehearsal, and Sample Collection [*Lauretta et al.,* 2017]. We present observations through Orbital C. Each phase included OpNav imaging in addition to science data collection. Starting with the acquisition of the first OSIRIS-REx images of Bennu in August 2018, every subsequent phase had observations that were useful, to varying degrees, for particle monitoring.

Observing circumstances varied from mission phase and within phases, as described in the following subsections. The changing circumstances mean that the sensitivity of the NavCam 1 imager to particles was not constant over the course of the mission. The size of the smallest detectable particles, assuming an albedo of 0.044, phase coefficient of 0.013

magnitude per degrees of phase angle, and nominal range to Bennu's center of mass (COM) is shown in Fig. 4 (see Results section for explanation of these parameters).

Particle detection methods also varied over the course of the mission phases in response to changing observing circumstances and evolving techniques, as detailed below. Biases introduced by the different methods are discussed in section 3.7 – Observation bias.

3.1. Approach phase

Bennu's spectral similarity to some active asteroids [*Lauretta et al.,* 2015] led the OSIRIS-REx team to survey the operational environment of Bennu for dust and satellites during the Approach phase in fall 2018 [*Lauretta et al.,* 2017]. Searches for dust along the orbit and anti-solar vector on 11 and 12 September 2018 at a range of $\sim 10^6$ km found no evidence of mass loss with a detection upper limit of 150 g s^{-1}. High density cometary tails or trails would have been visible at that range, but not discrete centimeter-size particles. A satellite search conducted over ten days in October and November 2018 at a range of ~3100 to ~150 km found no satellites larger than a diameter of 8 cm (for an albedo of 0.03, corresponding to the darkest material seen on the surface of Bennu) and 2 cm (for albedo of 0.15, corresponding to the brightest surface material) [*Hergenrother et al.,* 2019]. The reported detection limit used a Bennu disk-integrated phase function for the satellites which, as will be seen in the Phase Functions section below, was an incorrect assumption.
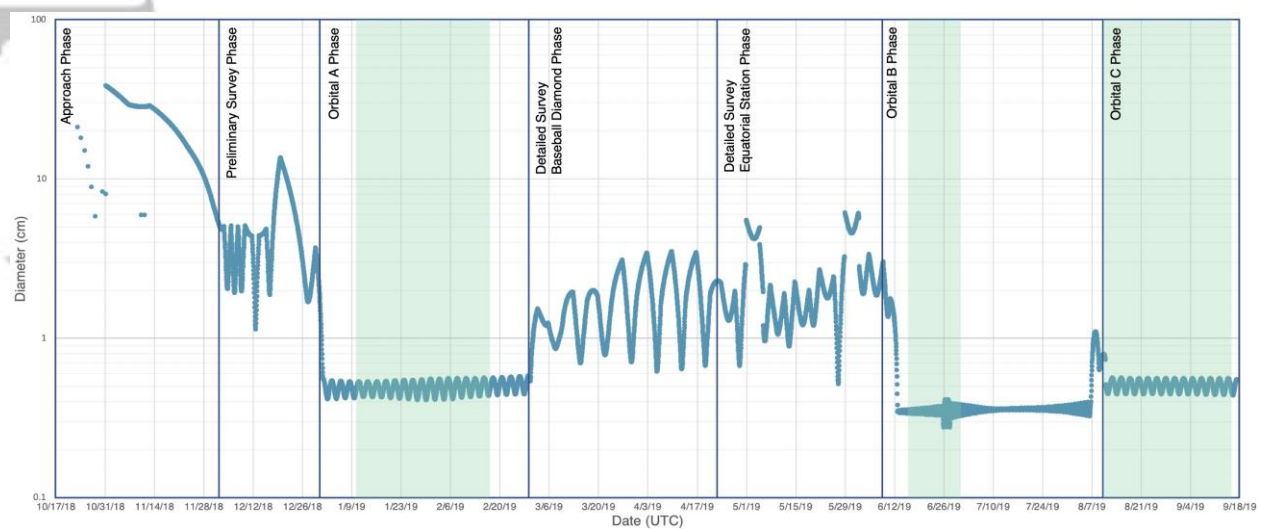

Fig. 4. Lower limit diameter of particles detectable by date. The detectable lower limit particle diameter is plotted for every hour between the start of the dedicated satellite search on 23 October 2018 and the end of Orbital C on 16 September 2019. Phase angles and ranges are to Bennu COM and particles have an albedo of 0.044 and phase coefficient of 0.013 mag/deg. The individual points in October and November are the OCAMS satellite searches. Mission phases are delineated and labeled. High cadence monitoring periods are shaded in green. Exposure times are valid for each observation. The detached 'V-shaped' features in Detailed Survey are due to the shorter exposure times used during the high phase angle flybys to prevent saturation of the image by stray light.

3.2. Preliminary Survey phase

Preliminary Survey began on 3 December 2018 and continued till 31 December 2018. The heliocentric range of Bennu decreased from 0.95 to 0.90 au during that time. OSIRIS-REx conducted five flyby maneuvers ranging from ~19 km to ~7 km of Bennu with phase angles spanning from ~5° to ~90°. While no dedicated observations for objects in the vicinity of Bennu were originally planned after the Approach-phase satellite searches, observations taken during Preliminary Survey were sensitive to particles within a few kilometers of Bennu.

During Preliminary Survey and all subsequent phases, NavCam 1 was the primary instrument for OpNav imaging. In Preliminary Survey, a pair of nadir-pointed 5-s-exposure NavCam 1 images was obtained every ~140 minutes during the daily 16-hour science observation windows. The images within each image pair were separated by ~30 s. The limiting magnitude for a particle in a 5-s NavCam 1 image is V~7.5.

A number of off-body returns from the OSIRIS-REx Laser Altimeter (OLA) instrument [*Daly et al.,* 2017] during Preliminary Survey may constitute the first evidence of particle ejection activity, although this remains to be confirmed [*Lauretta & Hergenrother et al.,* 2019]. After the discovery of particle ejection in January 2019, a small number of particles were later identified in Preliminary Survey NavCam 1 images. None of these could be linked with the OLA detections, which may not be surprising in that the instruments were not active at the same time. The particles in Preliminary Survey were found by identifying possible satellites in the GIANT visual aid plots and visual blinking of image pairs.

3.3. Orbital A phase

OSIRIS-REx transitioned into Orbital A on 31 December 2018 and spent most of the phase in a terminator orbit between 1.6 and 2.1 km from Bennu's COM with a mean orbital period of 62 hours. Orbital A phase was intended to be an OpNav-focused campaign. The nominal plan for OpNavs involved executing a mosaic of two fields every 2 hours. The mosaic was centered along the terminator plane of Bennu with sufficient overlap to allow Bennu to be imaged entirely within at least one field. Each mosaic field involved taking a short-long exposure pair of NavCam 1 images with respective exposure times of 1.4 ms and 5 s. The spacing between two overlapping fields was ~7 minutes. OpNavs were taken during the ~16-hour science observation window for a total of 16 to 18 long-exposure images per day.

The first recognized particle event was found in the 6 January 2019 OpNav images. An ad-hoc Mission Planning Board was convened to consider potential responses. One of the Board's findings was to augment the observation strategy to increase the likelihood of detecting and characterizing future events. The most expedient response was to continue the two field NavCam 1 mosaics with an increased frequency to every 30 minutes starting 10 January 2019. Images were taken over the ~16-hour window for a total of 66 long-exposure images per day.

Starting on 28 January 2019, the cadence of particle monitoring was increased again (hereafter, high-cadence monitoring). The nominal OpNav imaging cadence of two overlapping NavCam 1 mosaic fields every 2 hours continued, but with additional sets of two 5-s-exposure images at the spacecraft's default nadir attitude. Each set of two 5-s images

were 19.6 minutes apart, for a total of 5 sets of long-exposure pairs in between each OpNav mosaic. Images were taken over the ~16-hr window for a total of 98 long images per day.

The high-cadence particle monitoring during Orbital A completed on 18 February 2019, after which the mission reverted to OpNav imaging with two overlapping fields every 2 hours. Orbital A contained Bennu perihelion at 0.90 au on 10 January 2019. By the end of the high-cadence monitoring, the heliocentric distance had increased to 0.95 au.

Particles detected during Orbital A were found with an evolving set of methods and tools. The first event was found by visual blinking. By the end of Orbital A, with the introduction of GIANT, images were manually inspected after a possible object was noted in the GIANT visual aid plots.

3.4. Detailed Survey phase

The Detailed Survey Phase was conducted between 22 February 2019 and 8 June 2019 as the heliocentric distance increased from 0.99 to 1.28 au. While no dedicated high-cadence particle monitoring occurred during this phase, low-cadence monitoring continued with two NavCam 1 images every 2 hours. These images were targeted at nadir plus a 1° to 1.5° offset in the sunward direction. A pair of 5-s images were taken approximately 5 minutes apart. Maneuvers during Detailed Survey brought the spacecraft within ~2 km of Bennu COM and phase angles up to 130°. At high phase angles, the exposure times of the long NavCam 1 images were decreased to 2 s or 1.3 s to prevent saturation of the image by stray sunlight. The low cadence was a detriment to using the automated detection pipelines, so particles identified in this phase were found via manual blinking.

3.5. Orbital B phase

The spacecraft transitioned from performing Detailed Survey targeted flybys to orbiting Bennu on 8 June 2019. The Orbital B terminator orbit had a semi-major axis of ~0.9 km and orbit period of ~22.4 hours. Between 17 June 2019 and 1 July 2019, the spacecraft executed a dedicated particle monitoring campaign consisting of two overlapping mosaic fields. The mosaic fields were offset +/- 250 μrad along the terminator plane. The images at each offset target were spaced by roughly 193 s, and each field in the mosaic was spaced by 9.3 minutes. The mosaics were repeated on a cadence of ~25 minutes for 16.33 hours, such that 38 mosaics could be executed per day, or 152 long-exposure images per day. During this high-cadence monitoring, the heliocentric distance was between 1.30 and 1.32 au. A combination of visual inspection and the CSS automated detection pipeline was used to search all high-cadence Orbital B images.

3.6. Orbital C phase

The Orbital C mission phase between 6 August 2019 and 16 September 2019 was a dedicated particle monitoring phase added to the mission in response to the detection of the particle ejection phenomenon. The Orbital C phase provided an opportunity to monitor Bennu near aphelion (16 August 2019 at a heliocentric distance of 1.36 au). During Orbital C, OSIRIS-REx was in an orbit similar to Orbital A.

Nadir-pointed NavCam 1 images were acquired every 13 minutes over a 16.33-hour science window with a spacing between each image in the pair of ~138 s. The exposure time

was increased from 5 to 10 s to compensate for the increased Bennu-Sun range. This resulted in 76 long-exposure particle monitoring image pairs per science observation window, or 152 images per day, although a small fraction of Orbital C days experienced smaller image numbers due to other spacecraft activities. The CSS automated detection pipeline was the primary method of particle detection during Orbital C.

3.7. Observation bias

The variable observing circumstances and imaging cadences likely introduced biases in our ability to detect particles. Another factor was the evolution of detection tools resulting in improved detection capability with time. Sources of possible bias include:

- particles outside the NavCam 1 FOV owing to high velocity and/or large semi-major axis,

- particles remaining too close to Bennu and the saturated region around it to be imaged,

- particles in the shadow of Bennu,

- particles behind Bennu,

- particles in front of the illuminated part of Bennu,

- particles too faint to be detected, whether due to size or distance,

- particles or ejection events that were only visible during periods of little or no imaging,

- inability of automated detection pipeline to identify particles observable in fewer than four images.

The effects of these biases are likely time-variable and mission phase–dependent. Only the high-cadence imaging periods in Orbital A and Orbital C were optimized for both our software pipeline and visual detection tools. The continuous imaging of a single field centered close to Bennu with a cadence of 13 to 19.6 minutes for ~16 hours provided multiple opportunities to detect ejection events and nearby particles. Even in these imaging periods, however, events and particles occurring during the daily 8-hour span with no imaging would have been missed.

The Orbital A high-cadence imaging took place prior to the maturation of our automated detection pipeline. With slightly slower imaging cadence but a similar orbit to Orbital C, the detection pipeline should be efficient in detecting particles. Future work should identify particles missed by visual inspection during the high-cadence imaging period in Orbital A.

The Orbital B high-cadence period took place with the spacecraft in a lower orbit than in Orbital A and C. The need for two mosaic fields to cover the region around Bennu increased the repeat time for visiting each field. These factors resulted in many objects being visible in only a single pair of images, i.e., two detections per object, before leaving the NavCam 1 FOV. The automated detection pipeline was inefficient in detecting many particles because it requires a minimum of four detections per particle. Visual inspection

identified many two-detection tracks, but the poor imaging coverage meant few of these short tracks were linked into longer tracks or produced object trajectories.

Even during high-cadence imaging, observation biases affect our characterization of ejection events. Unlike a strongly collimated cometary jet [*Vincent et al.,* 2019], Bennu ejection events have a broad azimuthal launch cone [*Leonard et al.,* accepted, this collection] resulting in some fraction of ejected material being unobservable due to interference from the asteroid (e.g. particles in front of the sunlit hemisphere, behind the asteroid, or in shadow) or motion away from the spacecraft.

The analysis in Section 4 is based only on observed particles, as the particle population has not been corrected for the potential observational biases.

4. Results and Discussion

PSF fitting photometry was conducted on 668 particles resulting in 5368 separate measurements. *Chesley et al.* [in review, this collection] produced a catalog of particle detections and trajectories. We performed PSF fitting photometry on this catalog, resulting in successful photometric measurements for 5010 detections of 313 individual particles. Photometry was unsuccessful for detections located too close to stars, other particles, or Bennu. Photometry was also conducted on 387 detections of 384 particles identified as members of the following 2019 ejection events: 6 January, 19 January, 11 February, 19 April, and 18 June. Twenty-nine of these particles, with a single photometric measurement for each, were in common with the *Chesley et al.* [in review, this collection] catalog.

The photometry was used to determine the physical properties of the particles and ejection events. The steps for this approach, detailed below, are: (1) measure phase functions for a subset of particles with high-quality photometric datasets; (2) use the derived phase functions to determine the absolute magnitude, or intrinsic brightness, of the observed particles; (3) convert absolute magnitudes into sizes; (4) convert sizes into masses; (5) produce size frequency distributions for the largest events; (6) convert masses and ejection velocities into energies; (7) determine ejection masses and energies for individual events; and (8) measure both the mass loss rate and total observed mass loss from Bennu.

4.1. Phase function

A phase function describes the brightness of reflected sunlight from a particle as a function of its phase angle, where phase angle is defined as the Sun-particle-observer angle. Determining the phase function is the first step in estimating the size of the particles through the determination of the absolute magnitude of the particles. The absolute magnitude, H_V, is the apparent *V*-band magnitude a particle would have if observed from the Sun at a distance of 1 au and 0° phase angle. Photometry is normalized to particle ranges of 1 au from the Sun and observer (in our case, the NavCam 1 instrument) by the following.

$$V(1, 1, \alpha) = m_V - 5 \times log10(r\varDelta)$$

Here $V(1,1,\alpha)$ is the normalized magnitude, m_V is the apparent magnitude, *r* is the particle-Sun distance in au, and Δ is the particle-NavCam 1 distance in au. Phase functions can be

modeled a number of ways. Due to the lack of covering phase angles <70°, we fit the phase function with a straight line to produce a phase coefficient, or slope of the linear phase function.

In *Lauretta and Hergenrother et al.* [2019], phase functions were derived for three particles (designated P1, P2, and P3) with a phase coefficient of 0.018 ± 0.005 mag/deg. The uncertainty is the 1-sigma standard deviation. The new PSF fitting photometry results in a similar phase coefficient of 0.015 ± 0.006 mag/deg for P1 to P3 and agrees with *Lauretta and Hergenrother et al.* [2019]. The larger number of particles in *Chesley et al.* [in review, this collection] provided an expanded set of objects for phase angle analysis. While most particles have few photometric measurements or cover a small range of phase angles, we identified 15 "high-quality" particles, including P1 to P3, having a positive phase coefficient (increasing astronomical magnitude with increasing phase angle) and 40 or more photometric measurements spanning a phase angle range of >20° (Fig. 5, Table 1). This subset ensures the results are driven by the data and not spurious.

The phase coefficients range from 0.022 ± 0.002 magnitude per degree (mag/deg) for P2 to 0.001 ± 0.002 for P303. The phase coefficient of the high-quality particles is 0.013 ± 0.005 mag/deg where the error is the standard deviation of contributing values. This value is consistent within uncertainties with the 0.018 ± 0.005 mag/deg linear phase function found by *Lauretta and Hergenrother et al.* [2019], but much smaller than the 0.039 ± 0.001 and 0.040 ± 0.003 mag/deg found for disk-integrated Bennu [*Hergenrother et al.,* 2013; *Hergenrother et al.,* 2019].

The IAU H-G phase function is commonly used for disk-integrated asteroid photometry [*Bowell et al.,* 1989]. The H-G formalism resulted in unconstrained H_V values due to the lack of observed phase angles at <73°. A phase coefficient of 0.013 mag/deg produced unrealistic values of the G slope parameter. The IAU H-G formulation was found to be unsatisfactory for modeling the phase function of Bennu particles.

The particle phase functions are consistent with laboratory measurements of nearly centimeter-sized terrestrial rocks by *Muñoz et al.* [2017]. The measured terrestrial sample was a basaltic rock from Mount Etna with a 0.7-cm volume-equivalent sphere diameter with a dark, rough surface. We used the *Muñoz et al.* [2017] results available at the Amsterdam-Granada light scattering database [*Muñoz et al.,* 2012] to convert their photometric data from flux to astronomical magnitudes and from scattering angle to phase angle. Between phase angles of 70° and 120°, where the majority of Bennu particles were observed, the phase coefficient of the Etna sample was 0.006 mag/deg. The photometry of the Etna sample confirms that shallow phase coefficients at phase angles <120° is a common photometric characteristic of millimeter- to centimeter-sized solid objects.

Table 1. Summary of observations and phase functions for the best-observed particles. By "best-observed", we refer to a subset of 15 particles that were identified with >40 photometric observations over a phase angle range of >20°. The uncertainty in absolute magnitude contains –0.5 magnitude for any possible opposition effect.

| Particle Designation	Absolute Magnitude	Phase Coefficient (mag/deg)	Number of Photometric Observations	Phase Angle Range
P1	$42.84^{+0.13}_{-0.63}$	0.014 ± 0.001	105	$73.9° - 110.3°$
P2	$41.58^{+0.14}_{-0.64}$	0.022 ± 0.002	184	$77.3° - 107.1°$
P3	$42.90^{+0.25}_{-0.75}$	0.010 ± 0.002	92	$81.1° - 110.1°$
P15	$44.85^{+0.21}_{-0.71}$	0.018 ± 0.002	66	$80.5° - 117.5°$
P16	$44.57^{+0.14}_{-0.64}$	0.010 ± 0.001	47	$80.5° - 110.4°$
P41	$42.68^{+0.20}_{-0.70}$	0.010 ± 0.002	42	$74.9° - 110.9°$
P213	$44.39^{+0.25}_{-0.75}$	0.010 ± 0.003	42	$77.3° - 113.0°$
P247	$42.91^{+0.10}_{-0.60}$	0.007 ± 0.001	376	$78.9° - 108.3°$
P251	$44.18^{+0.06}_{-0.56}$	0.015 ± 0.001	42	$79.0° - 108.6°$
P266	$44.67^{+0.45}_{-0.95}$	0.015 ± 0.004	51	$87.0° - 112.1°$
P269	$43.38^{+0.28}_{-0.78}$	0.017 ± 0.003	45	$86.2° - 107.8°$
P273	$44.79^{+0.27}_{-0.77}$	0.010 ± 0.003	81	$80.5° - 114.3°$
P289	$43.74^{+0.22}_{-0.72}$	0.021 ± 0.002	101	$82.3° - 114.0°$
P303	$45.29^{+0.21}_{-0.71}$	0.001 ± 0.002	216	$81.2° - 106.3°$
P369	$45.03^{+0.81}_{-1.31}$	0.014 ± 0.008	45	$83.6° - 105.6°$
AVERAGE		0.013 ± 0.005		
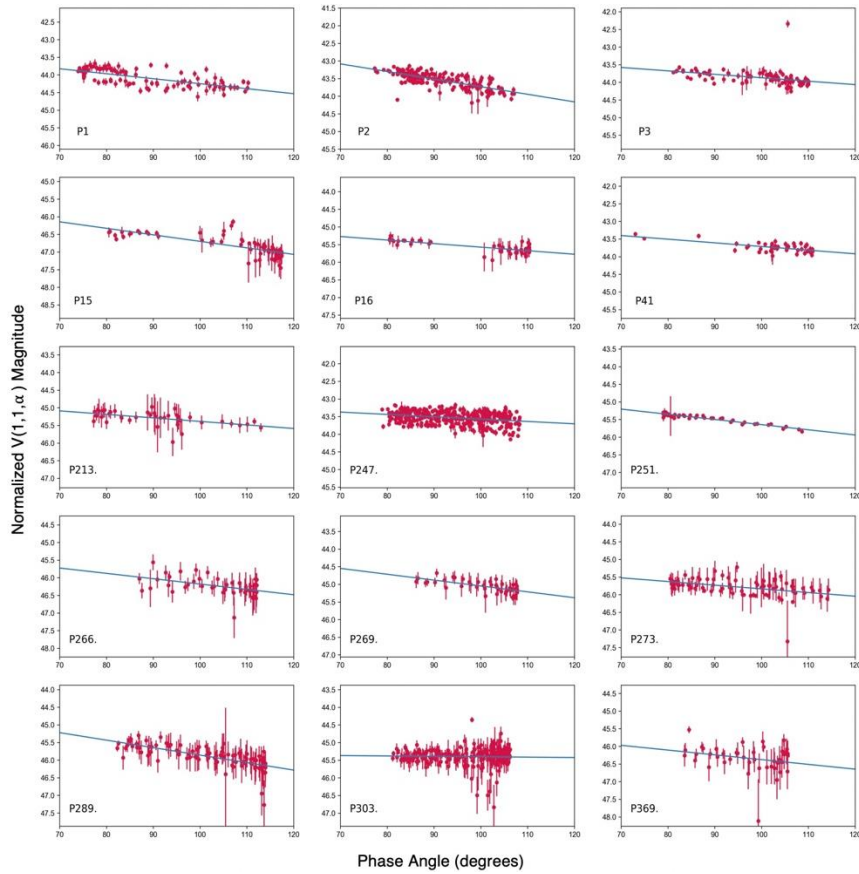
Fig. 5. Linear phase function of the 15 best-observed particles. The particles with the best observational coverage are those with 40 or more photometric measurements spanning a range of 20° or more in phase angle. All 15 particles were imaged during the Orbital phases and have phase angles between 70° and 120°. Weighted linear phase functions were fit to the particles resulting in the absolute magnitudes and phase coefficients (magnitudes per degree of phase angle) shown in Table 1

4.2. Particle Size

There are multiple ways to measure the size of a particle. The simplest would be to directly image a resolved particle. Unfortunately, due to the small size of the particles and the coarse plate scale (~58 arc minutes per pixel) of NavCam 1, no particles were resolved. At the mean distance to the asteroid during Orbitals A and C, the spatial 2-pixel resolution of NavCam 1 was ~100 cm., whereas the largest photometrically measured particle was P6 at 6.1 cm.

P120 was the nearest particle to the spacecraft with a trajectory solution. Its last observation was located only 158 m from the spacecraft. At that range, the spatial plate scale of NavCam 1 was 4.4 cm pixel^{-1}. If P120 were among the largest particles, it might have been resolvable. In practice, an object must subtend 2 pixels, or in this case 8.8 cm, to be considered resolved. The high phase angle of the observation (102.6°) also worked against its resolution: the object was less than half illuminated as seen by the spacecraft. Unfortunately, P120 is one of the smallest particles we detected with an absolute magnitude H = 48.2 corresponding to a diameter of 0.15 cm. In order to resolve a particle, it would need to be

both one of the largest and closest to the spacecraft, a combination that has not been observed.

We can also convert the photometry derived H_V values from the phase functions into diameters using

$$D_H = \frac{1.329 \times 10^8}{\sqrt{p_V}} 10^{-0.2\,H_V}$$

where D_H is the particle diameter in centimeters and p_V is the geometric albedo in the V band [*Fowler and Chillemi,* 1992; Pravec and Harris, 2007]. The area-to-mass ratios (η) produced by Chesley et al., [in review, this collection] provide another independent means to estimate particle size,

$$D_\eta = \frac{150}{\rho\eta}$$

where ρ is density of the particle (kg m^{-3}). Both methods assume spherical particles. If the particles are spherical and have typical Bennu values for p_V and ρ, then D_H and D_η should agree. But for a Bennu global mean p_V of 0.044 ± 0.011 [*DellaGiustina and Emery et al.,* 2019] and presumed Bennu meteorite analog ρ of 2000 ± 500 kg m^{-3} [*Macke et al.,* 2011; *Clark et al.,* 2011; *Hamilton et al.,* 2019], the D_H values are ~1.7x larger than the values of D_η (Fig. 6, a).
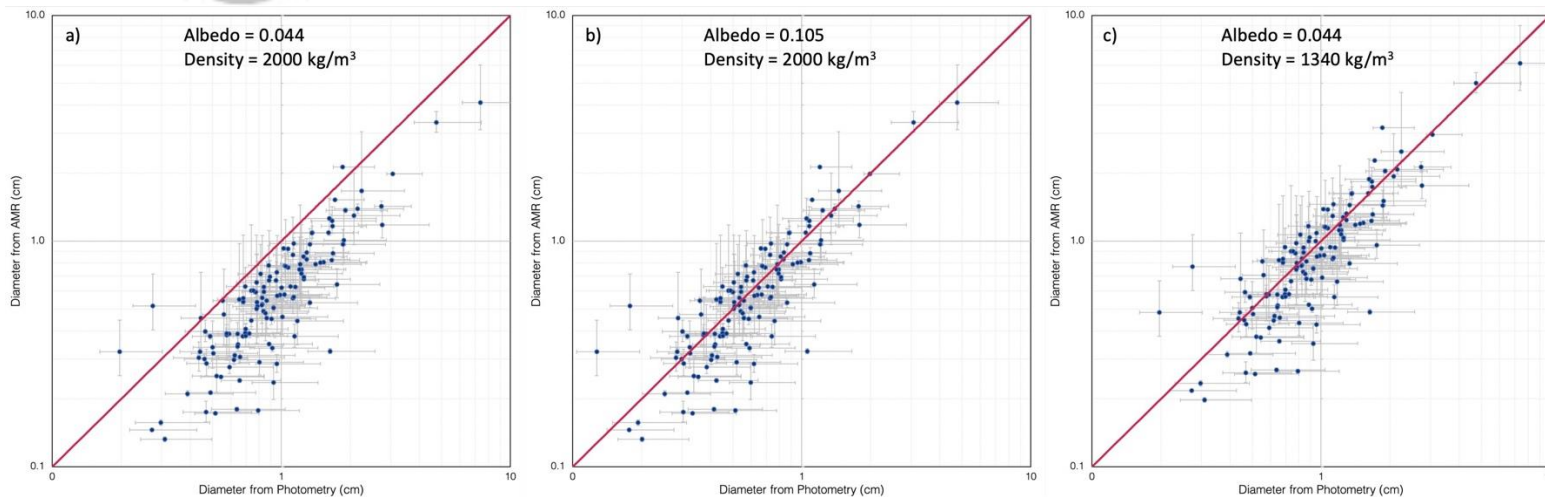

Fig. 6. Log-log comparison of particle diameters derived from photometry vs area-to-mass ratios. Diameters based on the absolute magnitudes (H$_V$) from PSF fitting photometry are compared to diameters based on area-to-mass ratios from OD analysis. (a) Density is fixed to the value of carbonaceous meteorite material (2000 kg m^{-3}) and the average albedo of Bennu (0.044). (b) Density is fixed at 2000 kg m^{-3} but best-fit albedo is solved for. (c) Albedo is fixed at 0.044 but best-fit density is solved for.

If we hold either the density or albedo fixed, we can find the best fit value for the other variable. The unfixed variable was incremented through a range of values. At each

increment, the reduced χ^2 was calculated. The best fit value was found when the reduced χ^2 was at a minimum. For a fixed density of 2000 kg m^{-3}, the best fit albedo is 0.105 (Fig. 6, b). Such a high albedo is unlikely as it is brighter than >96% of the surface of Bennu [*DellaGiustina and Emery et al.,* 2019] and would require a very small fraction of the surface to be responsible for particle production. Alternately, for a fixed global mean average of 0.044, the best fit density is 1340 kg m^{-3} (Fig. 6, c). This density is also unlikely as it is less than that of the Tagish Lake C2 chondrite, the lowest-density carbonaceous meteorite [*Brown et al.,* 2000]. Particles on the order of millimeters to centimeters should contain less pore space than the bulk asteroid resulting in particle densities greater than the 1190 kg m^{-3} bulk density measured for Bennu [*Scheeres et al.,* 2019].

The other assumption in the D_H and D_η equations is the sphericity of the particles. Chesley et al., [in review, this collection] dropped the assumption of sphericity and found that accounting for a non-spherical shape can lead to consistent size estimates between the D_H and D_η solutions. For an ellipsoid with semi-axes of $a \times a \times b$, density of 2000 kg m^{-3}, and albedo of 0.044, a mean axial ratio $r = b/a$ of 0.27 was found. This implies that the particles have a mean albedo and density similar to those measured for Bennu, but possess flake-like shapes, similar to findings from hypervelocity impact studies [*Michikami et al.,* 2016]. The mean axial ratio would be different for other assumed densities and albedos. For example, a less extreme axial ration would support particles with densities less than 2000 kg m^{-3} but greater than 1340 kg m^{-3}.

The rest of the analysis in this work will involve photometry based on the results found above. To derive H_V values, the phase coefficient 0.013 ± 0.005 mag/deg is extrapolated to 0° phase angle. Our observations and the laboratory work of *Muñoz et al.* [2017] could not produce a measurement of any opposition effect, or non-linearity due to back scattering at small phase angles. Telescopic observations at low phase angles of dark carbonaceous asteroids found a shallow opposition effect of 0.0 to 0.3 magnitudes but these objects have diameters of tens of kilometers or larger and may not experience an opposition effect similar to centimeter sized particles [*Shevchenko et al.,* 2008; *Muinonen et al.,* 2010]. Objects with sizes in the range of those observed around Bennu are found in the rings of Saturn [*Déau,* 2015]. The amplitude of the opposition effect of Saturn's rings ranges from ~0.2 to 0.5 magnitudes [*Franklin and Cook*, 1965; *Poulet et al.*, 2002; *Déau et al.*, 2018]. Our H_V error analysis includes the uncertainty in the phase function solutions, as well as non-linearity in the extrapolation to 0° phase angle due to a possible opposition effect up to 0.5 magnitudes (Table 1). We will continue to use a presumed Bennu meteorite analog ρ of 2000 ± 500 kg m^{-3} [*Macke et al.,* 2011; *Clark et al.,* 2011; *Hamilton et al.,* 2019] and Bennu mean surface p_v of 0.044 ± 0.011 [*DellaGiustina and Emery et al.,* 2019]. Following the lead of *Chesley et al.,* [in review, this collection], we will assume non-spherical particles and use a median b/a axial ratio of 0.27 for those particles without derived ratios. For diameters we use the equation for volume-equivalent spheres $\boldsymbol{D = 2\sqrt[3]{a^2 b}}$.

Particle Event Date	Time of Ejection (UTC)	Helio-centric Distance (au)	Number of Observed Particles[1]	Number of Particles with OD	Number of Particles with Photometry[1]	Source Latitude	Source Longitude	Local Solar Time	Derived Velocity Range (m/s)	Derived Particle Diameters (cm)	Derived Mass (g)[1]	Derived Translational Kinetic Energy (mJ)[1]	OD Ref.
Jan 06 near	$20:50:28 \pm 47s$	0.897	200+	117	180	$-75°\,^{-2.8°}_{+12.7°}$	$325.3°\,^{-10.3°}_{+18.9°}$	$15:22\,^{-00:36}_{+01:06}$	0.07-3.11	0.2-5.2	528^{+3106}_{-353}	77^{+427}_{-51}	2,5
Jan 06 far	$20:50:28 \pm 47s$	0.897	200+	117	180	$-57.3°\,^{-17.5°}_{+1.5°}$	$343.7°\,^{-14.7°}_{+3.8°}$	$16:35\,^{-01:05}_{+00:06}$	0.07-3.26	0.2-5.0	459^{+3489}_{-345}	62^{+448}_{-46}	2,5
Jan 19	$00:53:43 \pm 3s$	0.899	108	37	108	$19.925° \pm 0.9\,m$	$335.383° \pm 0.4\,m$	16:39:41	0.06-1.29	0.5-4.3	231^{+1670}_{-172}	29^{+209}_{-22}	2,3,4,5
Jan 26	$09:26:55 \pm 61s$	0.905	2	2	2	$-25.004° \pm 3.0\,m$	$11.369° \pm 1.4\,m$	22:00:25	0.11-0.12	0.9-1.0	$1.5^{+9.6}_{-1.3}$	$0.011^{+0.067}_{-0.009}$	3
Jan 29	$00:12:12 \pm 31s$	0.909	5	0	0	$17.9° \pm 0.9°$	$102.3° \pm 0.6°$	$18:51:06 \pm 69s$	0.11-0.18	n/d	n/d	n/d	4
Feb 04	$06:22:15 \pm 101s$	0.918	4	0	0	$33.4° \pm 22.3°$	$110.7° \pm 3.0°$	$18:50:55 \pm 234s$	0.12-0.21	n/d	n/d	n/d	4
Feb 05	$04:17:08 \pm 121s$	0.920	3	0	0	$41.2° \pm 0.6°$	$65.2° \pm 6.3°-$	$18:20:11 \pm 1653s$	0.18-0.31	n/d	n/d	n/d	4
Feb 08	$06:29:39.6 \pm 1s$	0.925	7	0	0	$41.55° \pm 0.05°$	$239.30° \pm 0.08°$	$12:44:39 \pm 20s$	0.36-0.44	n/d	n/d	n/d	4
Feb 08	$20:50:12.5 \pm 1.6s$	0.927	4	0	0	$31.38° \pm 0.04°$	$300.54° \pm 0.10°$	$01:00:06 \pm 36s$	0.19-0.20	n/d	n/d	n/d	4
Feb 11	$23:27:45 \pm 4s$	0.933	72	30	69	$15.065° \pm 0.7\,m$	$59.739° \pm 0.3\,m$	18:06:50	0.07-0.21	0.3-3.8	223^{+1498}_{-162}	$2.1^{+14.1}_{-1.6}$	2,3,4,5
Feb 15	$18:52:38 \pm 20s$	0.942	3	3	3	$8.017° \pm 0.7\,m$	$55.707° \pm 1.1\,m$	00:50:13	0.09-0.14	0.3-0.9	$0.83^{+6.04}_{-0.71}$	$0.004^{+0.027}_{-0.003}$	3
Apr 19	$01:58:08 \pm 32s$	1.137	22	18	20	$18.6° \pm 1.0°$	$225.2° \pm 2.5°$	$16:34:54 \pm 685s$	0.10-0.51	0.7-5.0	300^{+1451}_{-191}	21^{+110}_{-14}	4,5
Jun 18	$12:54:01 \pm 79s$	1.298	8	7	7	$16.3°\,^{-5.8°}_{+5.6°}$	$291.2°\,^{-6.1°}_{+7.2°}$	$17:32 \pm 00:07$	0.41-1.59	0.3-0.6	$0.63^{+4.18}_{-0.46}$	$0.14^{+0.96}_{-0.10}$	5
Aug 16	$10:51:59 \pm 74s$	1.355	2	2	2	$32.606° \pm 2.6\,m$	$248.834° \pm 1.5\,m$	20:12:26	0.14-0.18	1.2-1.4	$4.6^{+28.3}_{-3.8}$	$0.057^{+0.353}_{-0.048}$	3
Aug 23	$10:36:57 \pm 33s$	1.355	5	5	5	$48.741° \pm 10.0\,m$	$196.423° \pm 1.1m$	$18:07:17$	0.03-0.20	0.9-2.6	19^{+127}_{-16}	$0.07^{+0.43}_{-0.06}$	3,5
Aug 28	$18:35:28 \pm 195s$	1.353	5	5	5	$42.3728 \pm 17.0m$	$74.046° \pm 1.6m°$	05:06:20	0.13-0.17	0.2-0.3	$0.04^{+0.31}_{-0.03}$	$0.0005^{+0.0040}_{-0.004}$	3
Sep 05	$22:41:34 \pm 33s$	1.349	2	2	2	$-10.689° \pm 3.9\,m$	$319.315° \pm 2.3\,m$	13:34:56	0.06-0.06	0.6-1.2	$2.1^{+13.9}_{-1.7}$	$0.003^{+0.023}_{-0.003}$	3

Sep 13	22:40:36 ± 4s	1.342	30	22	20	-65.397° ± 0.3 m	20.595° ± 1.5 m	10:13:26	0.09-2.26	0.5-1.9	$16.0^{+124.7}_{-12.3}$	$4.3^{+32.4}_{-3.3}$	3,5
Sep 14	04:25:25 ± 25s	1.342	2	2	2	32.266° ± 1.8 m	181.255° ± 1.2 m	05:03:00	0.12-0.12	0.6-0.9	$1.1^{+7.8}_{-0.9}$	$0.007^{+0.054}_{-0.006}$	3

Table 2. Parameters for confirmed particle ejection events. This table summarizes our current knowledge for ejection events consisting of multiple particles which have been confirmed with orbit determined trajectories. Some of the events were previously characterized, and we show those data here for completeness, updated where our work has provided new values from additional detections and PSF photometry. In particular, the derived masses and translational kinetic energies for all events are new to this work, though some are refinements of previously published results. The references are: 1, this work; 2, Lauretta & Hergenrother et al. (2019); 3, Chesley et al. (in review, this collection); 4, Leonard et al. (accepted, this collection); and 5, Pelgrift et al. (accepted, this collection). Reference 1 (this work) is indicated in superscript by column; the other references apply to orbit determination (OD) and are indicated by row (i.e., event). 'm' in source latitude and longitude are meters. 'n/d' are values that are not determined.

4.3. Ejection event properties

Particles were imaged within minutes to days of ejection. The smallest events consist of only a single observed particle, while the largest contain hundreds of observed particles. Large events are defined as those producing 20 or more observed particles in a single image. This definition is based on detectability rather than the properties of the event. Events with 20 or more observable particles were easily detected via quick-look visual inspection of stray light–corrected images. Events with less than 20 particles required more rigorous visual inspection or use of the automated detection pipeline.

The large events on 6 January, 19 January, and 11 February 2019 are discussed in *Lauretta and Hergenrother et al.* [2019], *Leonard et al.* [accepted, this collection], and *Pelgrift et al.* [accepted, this collection]. A large 19 April 2019 event and several smaller events were analyzed in *Leonard et al.* [accepted, this collection] and *Pelgrift et al.* [accepted, this collection]. We present additional events observed through the end of Orbital C as well as further details for the previously reported events. Properties of all events with two or more particles are given in Table 2.

4.3.1. 6 January 2019 event

This event occurred one week after OSIRIS-REx entered its Orbital A orbit and four days before Bennu perihelion. The event, which was the first to be discovered, was noticed as an enhancement in the number of point sources seen just off the limb of Bennu, with the appearance of a large bright open star cluster.

The discovery was serendipitous for multiple reasons. The ejection event happened only ~6 minutes prior to the discovery image. At this point in the mission, OpNav images were taken every ~2 hours. The discovery image had an advantageous offset from nadir, allowing the detection of fast-moving particles. The 6 January event remains the largest observed event.

The event was captured in two images taken at 20:56:18 and 21:03:34 UTC. Over 200 particles have since been cataloged, though a smaller set enabled orbital (117 particles) and photometric (180 particles) analysis. The ODs were poorly constrained because particles were seen in only one or two images. This resulted in two possible solutions depending on whether the source was on the near or far side of Bennu. For this analysis, we analyze both solutions. Phase angles, Sun-particle ranges, and OSIRIS-REx–particle ranges for the 117 particles with OD solutions were used to estimate H_V values. For particles without OD solutions, the average phase angles and ranges of the 117 particles with OD solutions were used.

The fortuitous placement of the discovery image allowed particles with velocities up to 3.26 m s^{-1} to be imaged for the far solution and 3.11 m s^{-1} for the near solution. At the time of the event, Bennu COM was 0.897 au from the Sun and 1.66 km from the spacecraft at a phase angle of 92.6°. A single fast-moving particle is visible intersecting the edge of the NavCam 1 FOV, suggesting that more rapid material had already exited the image frame in the ~6 minutes that elapsed since the ejection time. Due to the shallower phase functions, PSF fitting photometry, and modeling of oblateness, this work's values for total observed mass and translational kinetic energy are lower than those reported in *Lauretta and*

Hergenrother et al. [2019] for this and the following events but within overlapping 1-sigma uncertainties [1800^{+900}_{-1520} g and 270^{+150}_{-225} mJ for the 6 January event].

4.3.2. 19 January 2019 event

The second particle event on 19 January 2019 was found via a visual inspection designed specifically for particle detection. Its discovery only two weeks after the first detected event confirmed mass loss at Bennu to be an episodic phenomenon. By 19 January, the Orbital A cadence of imaging had increased from image pairs every 2 hours to every 30 minutes.
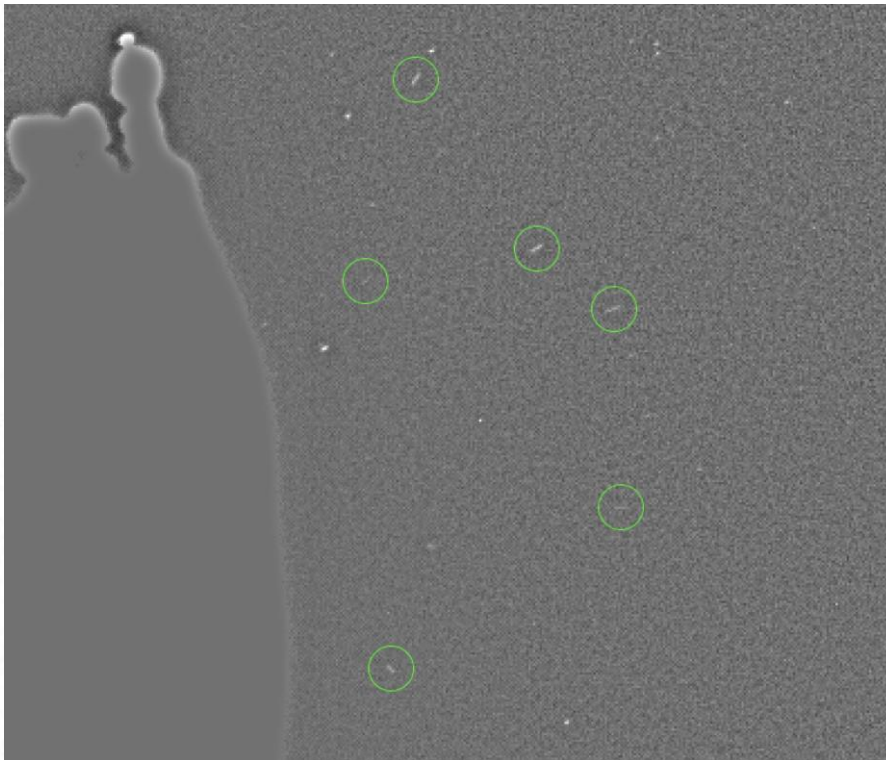
Fig. 7. Initial image of the 19 January ejection event. This is a crop of the image taken at 00:56:18 UTC which was ~2-3 minutes after the start of the event. Particles are trailed due to velocities up to 1.29 m s^{-1}. The edge of the NavCam 1 FOV is a few pixels beyond the right side of this image.

The first image at 00:56:18 UTC was taken within 2–3 minutes of the start of the event. Bennu COM was 0.899 au from the Sun and 1.97 km from the spacecraft at a phase angle of 92.1°. The first image was offset such that the ejection event was towards a field edge only ~300 pixels from the saturated edge of Bennu (Fig. 7). The subsequent image taken at 01:03:34 UTC was offset in the opposite direction, enabling a second detection of many of the fast-moving particles.

4.3.3. 11 February 2019 event

The third large event on 11 February 2019 was found after the Orbital A cadence had increased to nadir-pointed image pairs taken every 20 minutes. All three events were found through visual inspection of stray light–corrected images. The coverage of this event suffered due to the event being located close to the NavCam 1 FOV with a separation of ~370 pixels between the saturated region around Bennu and the FOV edge. Bennu COM was 0.933 au from the Sun and 1.64 km from the spacecraft at a phase angle of 91.6°. The first image at 23:39:44 UTC was taken ~12 minutes after the start of the event. High-velocity particles would have exited the field before the first image was acquired.

4.3.4. 19 April 2019 event

The 19 April 2019 event is unique among the multi-particle ejection events. It is the only event not observed during a dedicated particle monitoring period and orbital phase. Occurring while the spacecraft was maneuvering around Bennu, it is also the only large event observed at small phase angles. At the time of the event, Bennu was 1.137 au from the Sun, and Bennu COM was at a distance of 3.46 km and a phase angle of 20.1° from OSIRIS-REx.

Various factors may have contributed to observation biases for this event. The 2-hour cadence resulted in the first image taking place ~40 minutes after the time of ejection. Fast-moving particles would have already exited the NavCam 1 FOV. Bennu was brighter than in the orbital phases due to the lower phase angle, resulting in a larger region of saturation. It was also not centered in the FOV and rather close to one edge with only ~230 pixels between the saturated region and field edge (Fig. 8). The event particles were traveling in the direction of the close edge. With only 20 particles measured, the 19 April event may have been more massive than the 19 January event; however uncertainties are large. Further, had this event been imaged under the same observing conditions as the 6 January event, the detected mass may have rivaled or exceeded that event.

4.3.5. 13 September 2019 event

The 13 September 2019 event was first noted in an image taken during Orbital C on 13 September 2019 at 22:42:26 UTC. Three trailed high-velocity particles were observed in the first image, and a number of slower-moving particles were observed in a second image taken at 22:52:39 UTC. In total, thirty particles were identified of which 23 have photometric measures and 22 have OD solutions. Due to the high cadence of the imaging during Orbital C, 20 of the particles with OD solutions were observed in up to 28 images. At the time of the event, Bennu was 1.342 au from the Sun, and Bennu COM was at a distance of 1.76 km and 91.2° phase angle from OSIRIS-REx at the time of the event.
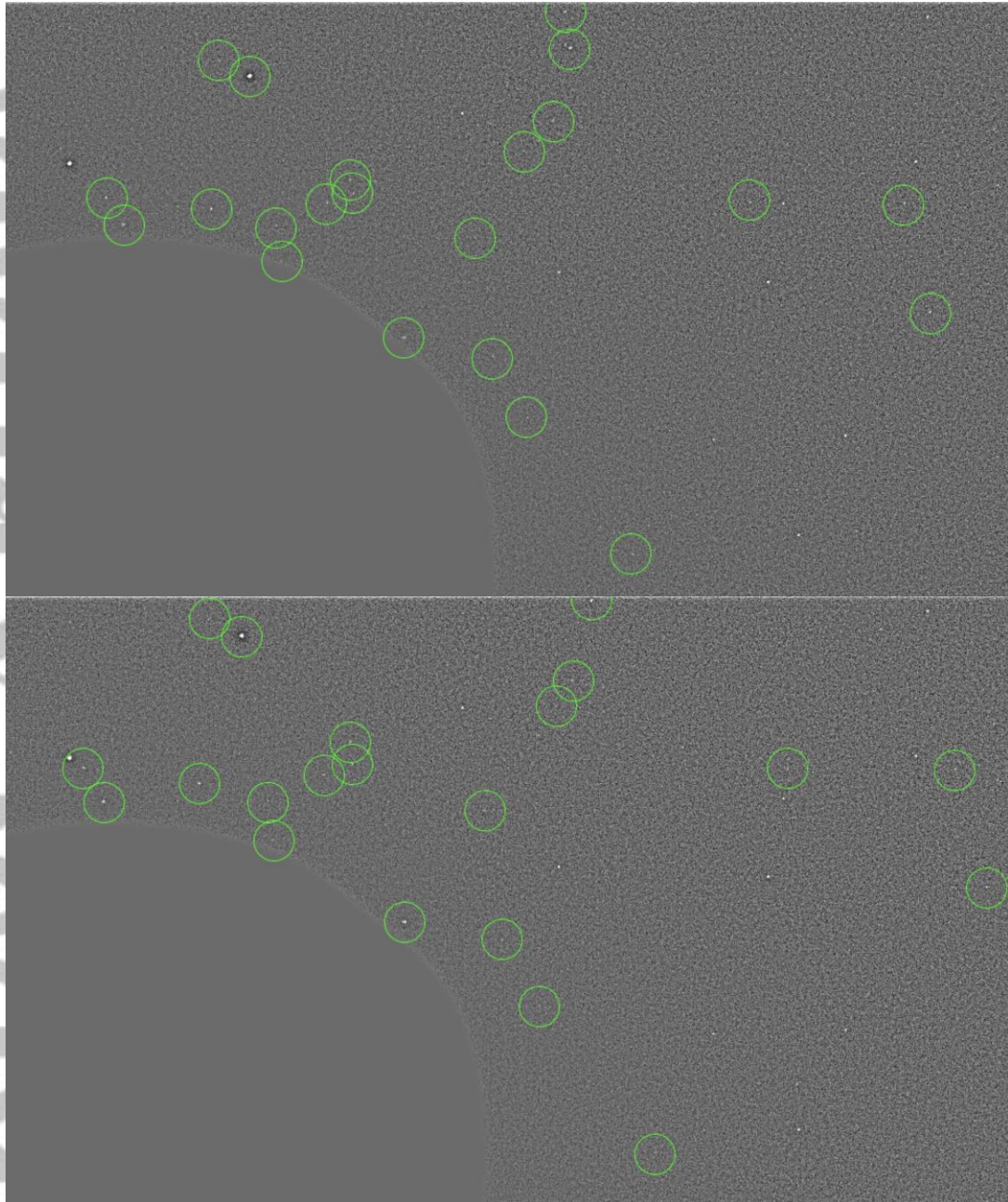
Fig. 8. Images of the 19 April 2019 ejection event. Twenty-two particles (circled in green) are seen in the pair of stray light–corrected images. (Top) NavCam 1 image taken on 19 April 2019 02:36:04 UTC. (Bottom) NavCam 1 image taken on 19 April 2019 02:39:56 UTC

4.3.6. Particle Rotation

One particle, P252, has more than 40 photometric measurements spanning a phase angle range of >20° but a negative phase coefficient of -0.014 ± 0.001 (Fig. 9 top). This suggests that its phase function is being contaminated by other effects such as a slow stable rotation or variable viewing aspect, the angle between the particle's rotation axis and observer line-of-sight. High-speed optical analysis of hypervelocity impact experiments has shown that fragments with diameters up to centimeters have rotation periods from 10^{-3} to 1 s [*Fujiwara and Tsukamoto,* 1981; *Fujiwara,* 1987; *Giblin,* 1998; *Kadono,* 2009; *Watson et al.,*

2019]. The NavCam1 exposure times were 5 or 10 s for all detected particles and would cover between 5 and 10000 rotations. Any rotation period shorter than 0.185 times the exposure length, corresponding to a 27 s rotation period for a 5 s exposure, would result in smoothing of the lightcurve amplitude [*Pravec et al.*, 2000]. The signal of a rotational lightcurve would be hidden by the many rotations within an image. Yet, P252 displays the clean signature of a partial rotational lightcurve with a gentle brightening trend, local maximum and gentle fading trend over a span of 8.1 hours (Fig. 9 bottom). If the lightcurve is due to rotation, then P252 has a single-axis rotation period on the order of 10s of hours.

The amplitude of the lightcurve informs the axial ratio of the particle. The relationship between the lightcurve amplitude and axial ratio [*Kwiatkowski et al.*, 2010] is

$$Axial\ Ratio\ (b/a) \geq \frac{1}{10^{0.4\ A(\alpha)/(1+s\alpha)}}$$

where *A(a)* is the observed lightcurve amplitude in magnitudes, *s* is the slope of the increase in lightcurve amplitude with phase angle, and *a* is the average phase angle of the observations (93° for P252). For *s* we use 0.015 magnitude per degree of phase angle as determined by *Zappala et al.* [1990] for carbonaceous asteroids. The lightcurve amplitude of P252 is greater than ~1.1 magnitudes. An amplitude of 1.1 magnitudes corresponds to a b/a axial ratio of 0.66. if the true amplitude of the lightcurve is twice this value, or 2.2 magnitude, it would correspond to a *b/a* axial ratio of 0.43 which is comparable to the median particle b/a ratio of 0.27 found by *Chesley et al.* [in review, this collection].

4.3.7. Energy Partition

The total energy of an ejection event is divided among a number of components in addition to the translational kinetic energy, including heat, melt, vaporization, comminution of the target, and rotational energy of the ejected particles [*Holsapple et al.*, 2002]. The fraction of the total energy partitioned into ejecting particles may only be on the order of <1 to 10s of percent [*Gault and Heitowit*, 1963; *Fujiwara and Tsukamoto*, 1980; *Waza and Matsui*, 1985]. In the case of the most energetic ejection event, the 6 January event, the total kinetic energy may be more than 100 times the observed translational kinetic energy (>7.7 J). Bottke et al. [in review, this collection] found that meteoroid impacts imparting kinetic energies up to 4000 J occur approximately ever 2 weeks over an entire Bennu orbit. If meteoroid impacts of this size are occurring routinely, then the observed ejecta represents a very small fraction of that energy.

For a 1 cm particle with ejection velocity of the order of 20 cm s^{-1}, a rotation period of 0.1 s corresponds to an approximate equipartition between translational and rotational kinetic energies [Chesley et al., in review, this collection]. Decreasing the rotation period to 10^{-3} s, as found in hypervelocity impact experiments [*Fujiwara and Tsukamoto*, 1981; *Fujiwara*, 1987; *Giblin*, 1998; *Kadono*, 2009; *Watson et al.*, 2019], results in a rotational to translational kinetic energy ratio on the order of 1000:1. A large fraction of the kinetic energy carried by the particles may be unobserved. This again suggests that the total kinetic energy of the ejection events may be orders of magnitude greater than the observed translational kinetic energy.
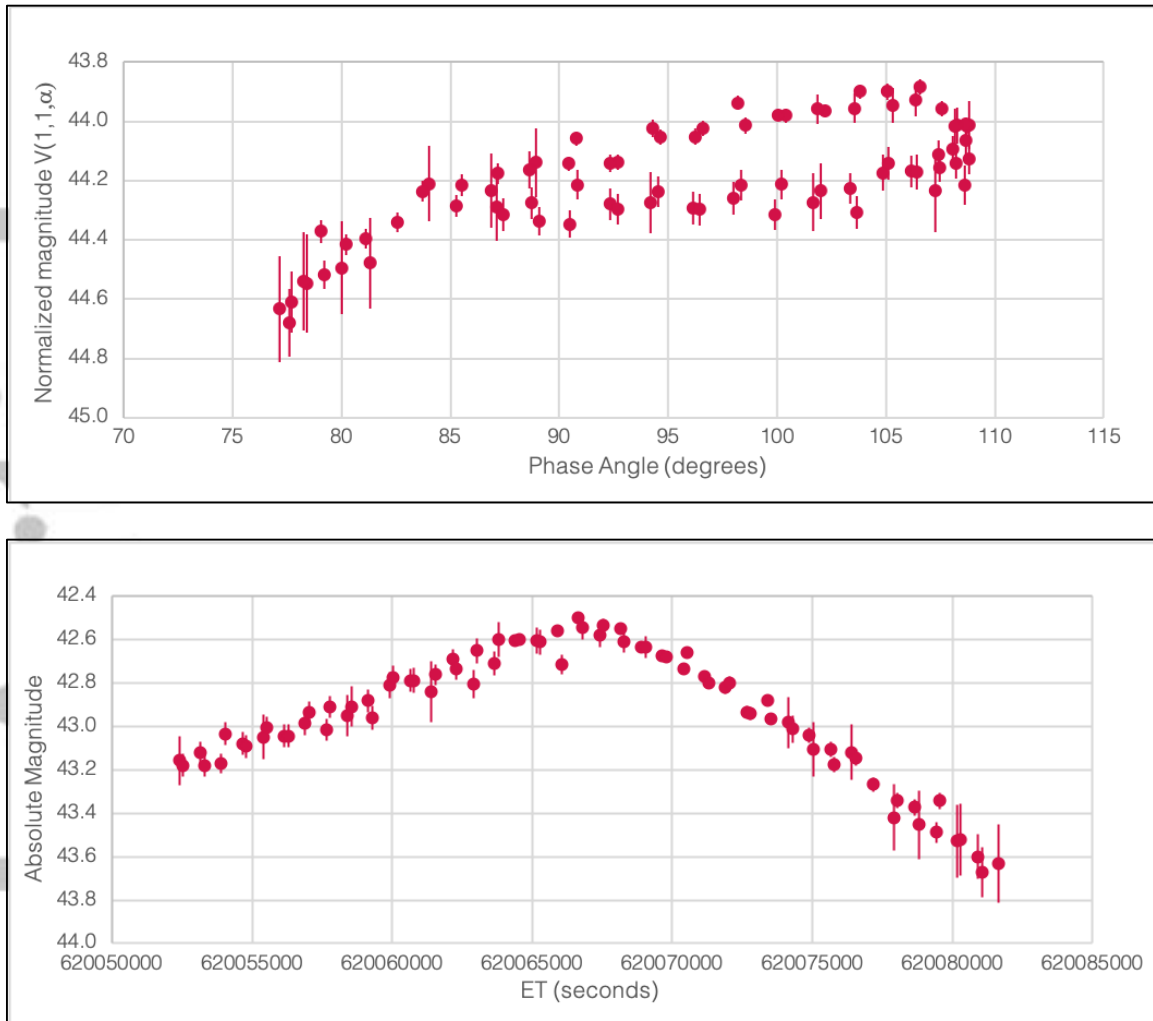
Fig. 9. Phase function and possible lightcurve for particle P252. (Top) Phase function for P252 showing a negative phase coefficient and structure. Data is normalized to a particle-Sun and particle-NavCam1 distance of 1 au. (Bottom) Photometry normalized to a phase angle of 0° and particle-Sun and particle-NavCam1 distance of 1 au. A phase coefficient of 0.013 mag/deg was used to normalize the brightness to a phase angle to 0°.

4.3.8. Size Frequency Distribution

The events on 6 January, 19 January, and 11 February 2019 have the largest number of particles observed, as well as the largest sample with derived photometry. Through the use of the PSF fitting photometry described above, coupled with the assumption of a geometric albedo of 0.044 and phase coefficient of 0.013 mag/deg, we converted the absolute magnitudes into corresponding diameters expressed in centimeters. The unbinned cumulative counts were used to compute the cumulative size frequency distribution (SFD) of the detected particles and the resulting best-fitting curves were identified (Fig. 10).
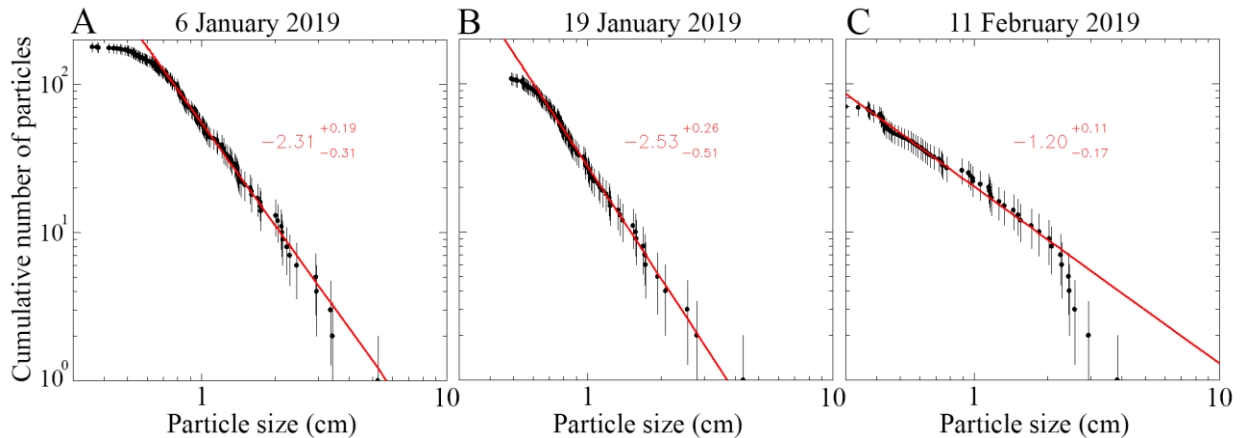
Fig. 10. The cumulative size-frequency distribution of the detected particles for the 6 January (A), 19 January (B), and 11 February 2019 (C) events

For the 6 January 2019 event (Fig. 10a) the best-fitting curve is a power law characterized by an index of $-2.31^{+0.19}_{-0.31}$, computed in the size range of 0.7 to 3.5 cm. Below 0.7 cm, the distribution bends, departing from the power-law trend. Given the large number of particles with sizes smaller than 0.7 cm, such a break in the SFD could be a real result of intrinsic surface processes that deplete the smallest sizes when they form. Nevertheless, a more likely possibility is that such rollover may be the result of an observation bias, where fewer smaller particles are identified, in a similar fashion to the pixel resolution limit when pebbles are identified on surfaces (e.g. *Pajola et al.* [2017]).

For the 19 January 2019 event, instead, the best fit derived is a power-law curve with index $-2.53^{+0.26}_{-0.51}$, computed in the range of 0.7 to 2.8 cm (Fig. 10b). As for the previous case, there is a rollover towards the smaller sizes that occurs below 0.7 cm. The clear departure from the power-law trend suggests that this is the result of the observation bias towards the smallest sizes mentioned above.

For the 11 February 2019 event, we derived a power-law curve with index $-1.20^{+0.11}_{-0.17}$ as the best fit between 0.3 and 2.4 cm in size. Figure 10c shows that in this case no rollover appears, but the index of the distribution is much shallower than the two previous ones.

Even if we do not consider the shallow SFD below 0.7 to 1.0 cm (observed for the 6 and 9 January events), whose origin is still debated and which may be attributable to observation biases, the particularly shallow power-law indices that we obtain for all three events (from -2.6 to -1.2) suggests a scarcity of small particle sizes on asteroid Bennu hinting that depletion phenomena may occur on the surface before the particle ejection. Either fine regolith material is not being produced by processes such as thermal fracturing [*Molaro et al.,* in review, this collection], or fine material is being removed after formation by electrostatic lofting [*Hartzell et al.,* in review, this collection] or some other process. A scarcity of small particles sizes was found on Ryugu [*Jaumann et al.,* 2019] which is a similar sized carbonaceous asteroid to Bennu and may also experience a depletion phenomenon.

The potential meteor flux associated with particles ejected from Bennu has been calculated by *Ye* [2019] to be very low, with Zenith Hourly Rates of <<1 for most years. The

low entry speed of 6 km s^{-1} further limits the detection of any meteors from Bennu. On the other hand, the SFDs of Bennu particles, at least from the 6 and 19 January events, have power-law indices consistent with those of the Geminid and Quadrantid meteor streams (cumulative SFD power-law index ~-2.2, [*Blaauw et al.,* 2011]). Interestingly, both meteor streams are associated with apparent asteroids: the Geminids with (3200) Phaethon [*Whipple,* 1983] and the Quadrantids with (196256) 2003 EH$_1$ [*Jenniskens,* 2004], although the latter could be an intermittently active comet.

The population of large particles around the nucleus of comet 103P/Hartley 2 discovered by the Deep Impact spacecraft showed power-law slopes of -6.6 to -4.7 [*Kelley et al.,* 2013; *Hermalyn et al.,* 2013], much steeper than those of Bennu's particles. The range of sizes for 103P particles is from centimeters up to ~2 m. The large particles of 103P are most likely lifted by volatile outgassing from the comet and represent the largest sizes of particles that are launched from the nucleus. The steep SFD is a natural consequence of the size-dependent particle ejection due to cometary outgassing. Therefore, the distinctly different SFD power-law slopes of Bennu particles and 103P particles are strong evidence of different particle creation and/or ejection mechanism on these two objects.

4.3.9. Production Rates

We can directly compare particle ejection mass and translational kinetic energy rates between the Orbital A mission phase, which included Bennu perihelion, and the Orbital C mission phase, which was similar in geometry and included Bennu aphelion (Fig. 11). The calculated rates use the following parameters: albedo of 0.044, density of 2000 kg m^{-3}, and phase coefficient of 0.013 mag/deg. During the 20 days of Orbital A high-cadence monitoring, the total observed ejected particle mass was 321 g with a daily average of 15.3 g. The total observed translational kinetic energy was 3.4 mJ with a daily average of 0.164 mJ. During the 30 days of monitoring in Orbital C, the total observed ejected mass was 141 g, or with a daily average of 4.7 g. The total observed translational kinetic energy was 5.1 mJ, or 0.170 mJ per day. Note that here we exclude the large events on 6 and 19 January, as they were not captured by high-cadence monitoring.

The daily mass ejection rate decreased by ~70% between perihelion and aphelion, while the daily translational kinetic energy rate stayed approximately unchanged. The particle ejection mechanisms proposed by *Bottke et al.* and *Molaro et al.* [in review, this collection]—meteoroid impacts and thermal stress fracturing, respectively—may explain the decrease in daily ejection rate. The Bottke et al. meteoroid model predicts a factor of 5 decrease in meteoroid flux between perihelion and aphelion. The Molaro et al. [in review, this collection] thermal fracturing model predicts a 50% decrease in peak stresses between perihelion and aphelion, but does not predict the release of rapid particles (>0.2 m s^{-1}) as observed near aphelion in the 13 September event (up to 2.3 m s^{-1}). A combination of the two mechanisms, however, may explain the apparent gentle decrease in activity with heliocentric distance because it would allow for the occasional high-energy meteoroid impact event superimposed on an overall decreasing trend.
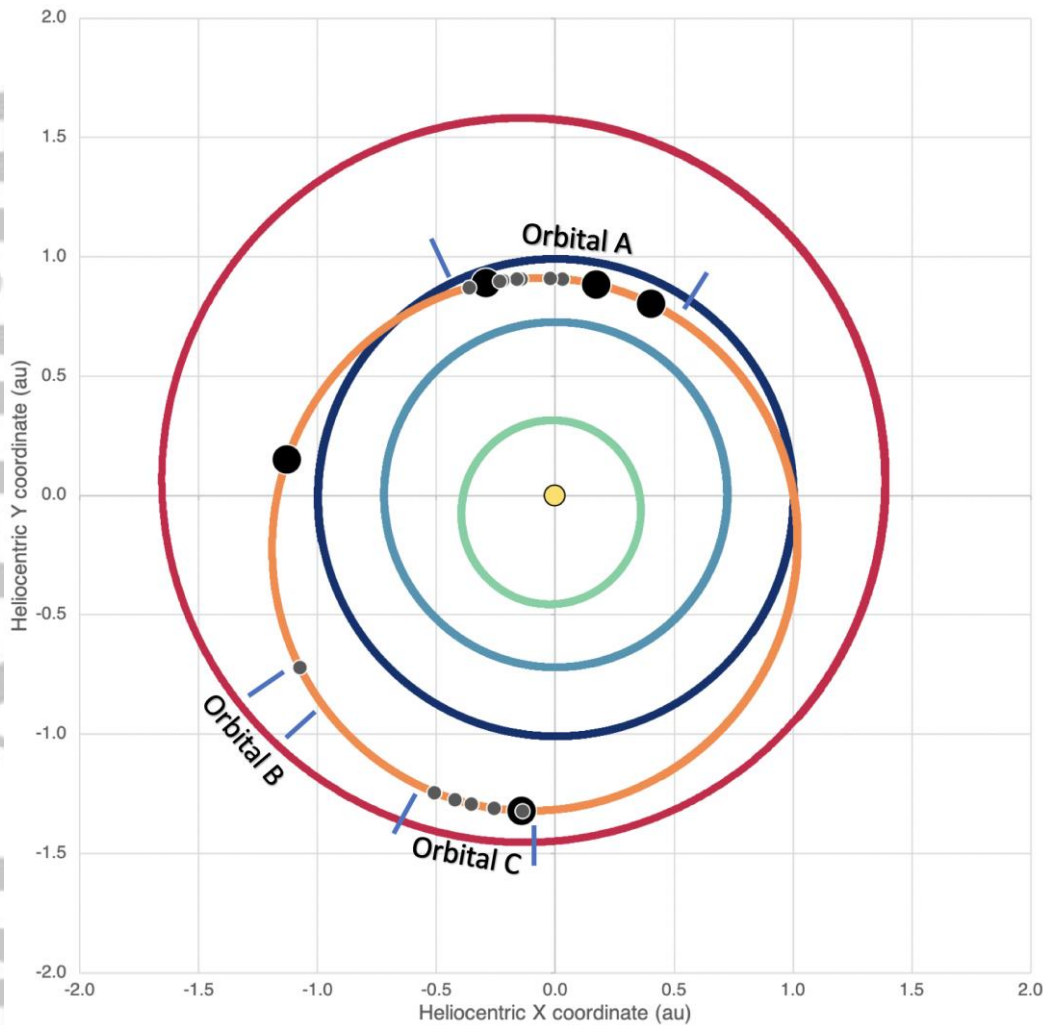
Fig. 11. Distribution of multiple particle ejection events around the orbit of Bennu. The orbit of Bennu is in orange. The large black circles denote ejection events with 20 or more particles. The small grey circles denote ejection events with between 2 and 19 particles. The times of the dedicated particle monitoring phases (Orbital A, B, and C) are shown. The Sun and the orbits of Mercury, Venus, Earth, and Mars are also shown.

The comparison between Orbital A and C likely suffers from small number statistics. The mass and energies observed during both the periods were heavily affected by a single large ejection event. The 11 February event contributed ~84% of the ejected mass and ~77% of the translational kinetic energy during that period. During Orbital C, the 13 September event contributed ~21% of the mass and ~90% of the translational kinetic energy.

The most energetic dates, in decreasing order by derived energies, were 6 January 2019 (77 mJ), 19 January 2019 (29 mJ), 19 April 2019 (21 mJ), 13 September 2019 (4.3 mJ), and 10 December 2018 (1.7 mJ). The most massive dates, in decreasing order by derived masses, were 6 January 2019 (528 g), 19 April 2019 (300 g), 19 January 2019 (231 g), 11 February 2019 (223 g), and 10 December 2018 (145 g). All of these dates involved large ejection events with the exception of 10 December. That date involved a single particle (P6), which may be the largest observed particle at 6.1 cm. While no other particles were observed on that date, the spacecraft was located at a range of 17 to 18 km with phase angles between 74° and 84°. Particles smaller than ~4 cm would have not been visible. A multi-particle ejection event on 10 December cannot be ruled out.
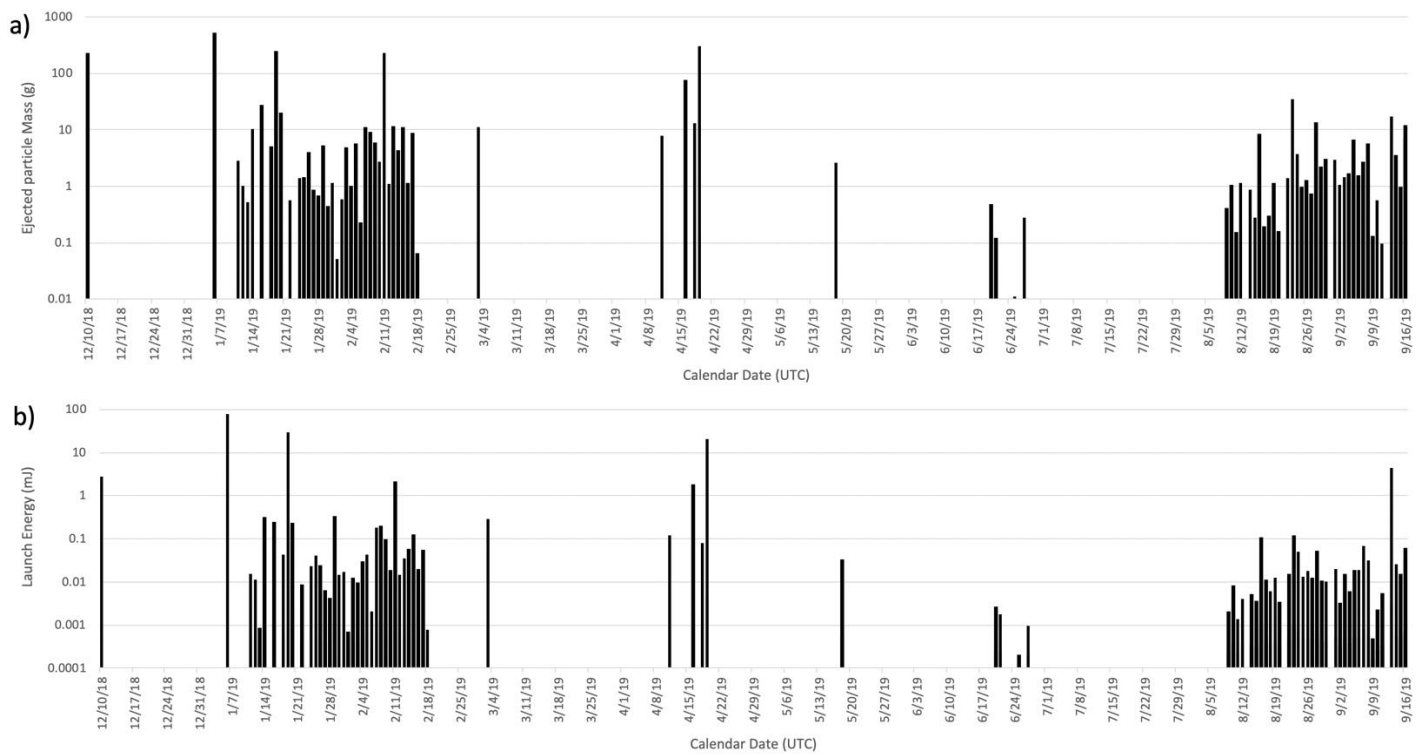
Fig. 12. Total observed mass and translational kinetic energy of ejected mass per day. The high cadence particle monitoring periods in Orbital A (January/February 2019) and Orbital C (August/September 2019) are evident as times with consistent detections of particle activity. The Orbital B high cadence period in June 2019 is poorly represented here since the spacecraft's close orbit around Bennu resulted in few long tracks or trajectories. Low cadence monitoring occurred between the Orbital A/B/C periods resulting in a lower detection efficiency.

The total observed mass loss from Bennu during our observation period (10 December 2018 to 16 September 2019) was 1963 g. This is a lower limit because the spacecraft spent most of that duration at poor observing geometries or not monitoring for activity. Fig. 12 shows the observed daily ejected mass and translational kinetic energy by calendar date (0 h UTC to 0 h UTC). The Orbital A (January–February) and Orbital C (August–September) periods are obvious as an ejection was detected nearly every day during those periods. The gaps in Orbital C are days with little or no particle imaging. Orbital B (June) produced few particles with trajectories. While many tracks were identified in Orbital B, most had only two detections due to the low orbit and poor imaging cadence.

We calculated a first-order estimate of the total mass of ejected particles by correcting for time not spent monitoring for particles or when the spacecraft was poorly placed to observe particles. Over an entire orbit, we find that Bennu releases on the order of 10^4 g corresponding to a production rate of 10^{-4} g s^{-1}. Most of the particles re-impact the surface of Bennu. *Chesley et al.* [in review, this collection] found that 15% of the particles entered hyperbolic escape trajectories. *Pelgrift et al.* [accepted] reported that 25% of particles in 11 examined ejection events escaped Bennu. To calculate the total mass escaping Bennu, we

combined the masses of the escaping particles with ejection velocities greater than escape velocity (0.2 m s^{-1}) [*Scheeres et al.,* 2019]. The total observed escaping mass was 584 g or ~30% of the total.

The resulting mass loss rate is orders of magnitudes less than the rate experienced by (3200) Phaethon near its perihelion (10^2 to 10^3 g s^{-1}), however Phaethon is larger than Bennu and travels closer to the Sun (*Hui and Li,* 2016). If we conservatively assume that the ejection process is roughly proportional in strength to the heliocentric distance (r^{-2}), then normalizing Bennu's perihelion distance (0.895 au) to Phaethon's (0.140 au) produces activity (0.140 au / 0.897 au)$^{-2}$ or ~41 times stronger. If we normalize mass loss for larger surface area (D^2) of Phaethon (6.2 vs 0.49 km diameter) [*Taylor et al.,* 2019], then Bennu's activity would increase by an additional (6.2 km / 0.49 km)^2 or ~150 times. If we scaled up the size of Bennu to match Phaethon and moved it to Phaethon's perihelion distance, its mass loss rate could increase to ~1 g s^{-1} which is within 0.1-1% of what is observed at Phaethon. If the ejection process increased at r^{-3} or r^{-4}, as is common with comets [*Green et al.,* 2001], the activity at 0.14 au would rival that experienced by Phaethon.

4.3.10. Remote observability of events

Mass loss from comets and active asteroids is usually detected as cometary-like morphology, such as comae and tails, or as a brightening of the object. We analyzed photometric observations published by the Minor Planet Center (MPC) and *Hergenrother et al.* [2013] to search for signs of past mass loss activity from Bennu. Since its discovery in 1999, Bennu was primarily observed during its close approaches to Earth in 1999, 2005/2006, and 2011/2012.

Due to the variable quality of some submissions to the MPC, we limit the photometry to observers contributing two or more nights of observations. This allows us to determine for each observer a correction factor, a relative offset to the *V* magnitude linear phase function in *Hergenrother et al.* [2013]. This factor corrects for observer-specific biases such as the use of different filters, including the use of no filter, and CCD detectors with varying quantum efficiencies. The observers, denoted by MPC code and observatory name, and their correction offsets are the following: 046 Klet Observatory, +0.5 magnitude offset; 428 Reedy Creek, -0.14 magnitudes; 703 Catalina Sky Survey, +0.26 magnitudes; 848 Tenagra Observatory, -0.01 magnitudes; 859 Wykrota Observatory-CEAMIG, -0.65 magnitudes; 950 La Palma, +0.91 magnitude; E12 Siding Spring Observatory, +0.31 magnitudes; and H01 Magdalena Ridge Observatory, +0.42 magnitudes.

The resulting photometry is normalized for phase angle, heliocentric and geocentric distance by

$$H_V = m_V - 5 \times log10(r\Delta) - (\beta\alpha)$$

where m_V is the apparent magnitude, r is the heliocentric distance in au, Δ is the geocentric distance in au, α is the phase angle in degrees, and β is 0.04 magnitudes per degree of phase angle, the disk-integrated phase coefficient for Bennu [*Hergenrother et al.,* 2013]. A secular lightcurve [*Ferrin,* 2005] shows the intrinsic activity of an object around its orbit and is produced by plotting the normalized photometry against time relative to perihelion. Fig. 13 shows the secular lightcurve for the 1999, 2005/2006, and 2011/2012 orbits. Coverage in 1999 spanned only a few tens of days around 60 days before perihelion. The coverage in

2005/2006 and 2011/2012 spanned from ~100 days before perihelion to near aphelion. All photometry falls within ±0.8 magnitude of the mean and shows no apparent enhancement in brightness.
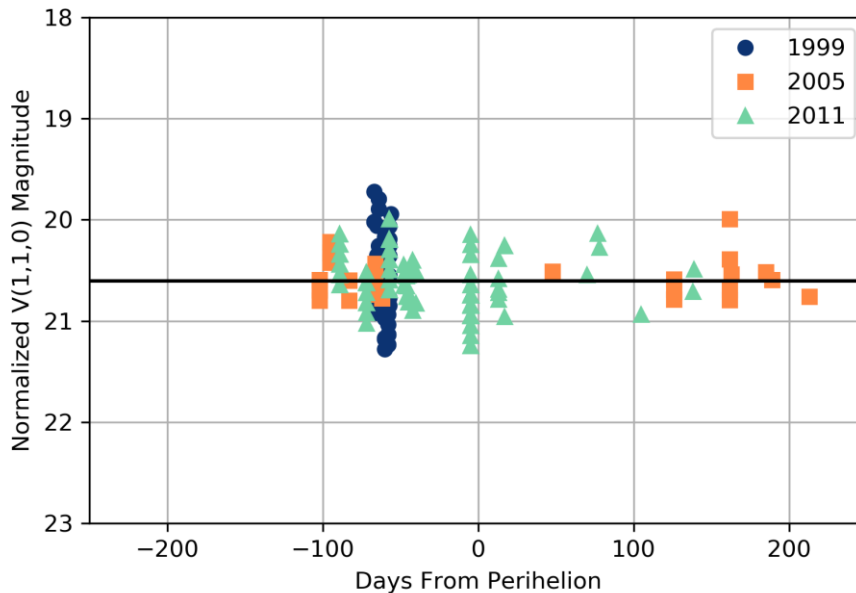

Fig. 13. Secular lightcurve of Bennu from ground-based photometry. Photometry data from the Minor Planet Center observations database and Hergenrother et al., [2013] are normalized to geocentric and heliocentric distances of 1 au and a Bennu disk-integrated phase coefficient of 0.04 mag/deg. Observations from the close approaches in 1999, 2005, and 2011 are plotted relative to time from perihelion. No obvious increases in brightness due to mass loss activity is seen.

No known ground-based or near-Earth telescope observations were made of Bennu during the time of the observed activity. The last observation reported to the MPC was on 15 May 2018. At the time of the first known particle on 10 December 2018, Bennu was observable at a solar elongation of 62° but a faint V ~ 22.7 magnitude. Bennu peaked in brightness at V ~ 22.2 in February but had faded to V ~ 24.1 by the end of Orbital C making it too faint for the all-sky asteroid surveys to detect during its observed time of activity.

Approaching from the other direction, what size particle ejection would be detectable by telescopic observation? The average diameter of Bennu is 490.06 m [*Barnouin et al.,* 2019] resulting in a projected area at 0° phase angle of 1.9×10^9 cm^2. The total projected area of the spherical particles observed in the largest ejection event on 6 January was ~170-190 cm^2, roughly the size of a CD jewel case. A sudden increase in brightness of 0.1 magnitudes, or 9.6%, should be noticeable when conducting high signal-to-noise lightcurve measurements of Bennu. Such an increase requires the release of particles with a total projected area of 1.8×10^8 cm^2, or ~10^6 times the projected area of the 6 January event. The detection of particle events at Bennu is thus beyond the capability of remote optical telescopes, meaning that similar activity may be occurring undetected at other near-Earth objects.

5. Conclusions

Near-Earth asteroid (101955) Bennu, the target of the OSIRIS-REx mission, is an active asteroid ejecting millimeter- to centimeter-sized particles. Activity has been observed from a month before perihelion to a month after aphelion and may continue throughout the current inbound part of Bennu's orbit. Activity appears to decrease gently between perihelion and aphelion. Biases may have been introduced by the variation in detection methods and observing circumstances over the course of the observations. Future work may address some of these biases and allow a better understanding of the properties of the particle population and the responsible mechanisms.

The phase functions of the particles are unlike those seen for asteroid surfaces. The phase coefficient of 0.013 mag/deg is consistent with terrestrial millimeter- to centimeter-scale rocks [*Munoz et al.,* 2017]. The particles are among the smallest discrete objects observed above Earth's atmosphere. The characterization of particles ejected from Bennu fills a gap of direct measurement between small, micron-sized particles and large, meter-sized and larger particles. Micron to hundred micron–sized particles are often modeled from their light scattering properties in the visible wavelengths; particles in the hundred microns to millimeters size range can be observed from their thermal emission (e.g. *Kolokolova et al.* [2004]); and macroscopic particles of more than a meter in size can be inferred from small impact craters on large asteroids [*Marchi et al.,* 2015]. Direct observations of centimeter to decimeter particles in interplanetary space are scarce. The only currently available measurements came from 67P and 103P [*Hermalyn et al.,* 2013; *Davidsson et al.,* 2015; *Levasseur-Regourd et al.,* 2018]. Bennu joins Phaethon as asteroids with active particle ejection and suggests that asteroids, like comets, can also be an important source of interplanetary dust.

The mass loss rate of Bennu is many orders of magnitude smaller than those measured for other active asteroids. The largest ejection events are themselves many orders of magnitude smaller than required to be detected by Earth-based or near-Earth-based telescopes. The future study of this phenomenon may require study by spacecraft in situ.

While no prior mission has detected particle activity around their target asteroids, almost all asteroid missions have searched for satellites and other near-asteroid hazards. The Dawn mission was sensitive to satellites as small as 3 m around V-type (4) Vesta [*McFadden et al.,* 2015] and 12 m around carbonaceous Cg-type (1) Ceres [*McFadden et al.,* 2018]. Hayabusa1 surveyed for satellites as small as 1 m around S-type NEA (25143) Itokawa [*Fuse et al.,* 2008] while the Hayabusa2 mission would have seen objects down to a 10 cm diameter around carbonaceous Cg-type NEA (162173) Ryugu [*Watanabe et al.,* 2019]. The OSIRIS-REx Approach phase satellite search could have detected particles as small as ~5 cm. The largest particles observed at Bennu, as calculated using PSF fitting photometry, are ~6 cm in diameter and they are rare occurrences. This is smaller than the limiting size for the satellite searches conducted by other missions. The null detection of particles at other asteroids does not preclude the existence of similar unresolved activity at those bodies.

Acknowledgments, Samples, and Data

References

Astropy Collaboration, Robitaille, T. P., Tollerud, E. J., Greenfield, P., Droettboom, M., Bray, E., … Streicher, O. (2013), Astropy: A community Python package for astronomy, Astronomy and Astrophysics, 558, id.A33. doi:10.1051/0004-6361/201322068.

Astrophy Collaboration, Price-Whelan, A. M., Sipõcz, B. M., Günther, H. M., Lim, P. L., Crawford, S. M., … Astropy Contributors. (2018), The Astropy Project: Building an open-science project and status of the v2.0 core package, The Astronomical Journal, 156, id.123. doi:10.3847/1538-3881/aabc4f.

Barnouin, O. S., Daly, M. G., Palmer, E. E., Gaskell, R. W., Weirich, J. R., Johnson, C. L., … D. Lauretta, D. S. (2019), Shape of (101955) Bennu indicative of a rubble pile with internal stiffness. Nat. Geosci., 12, 247–252. doi:10.1038/s41561-019-0330-x.

Bertin, E. (2010), SCAMP: automated astrometric and photometric calibration, Astrophysics Source Code Library, record asci:1010.063.

Bertin, E., & Arnouts, S. (1996), SExtractor: software for source extraction, Astronomy and Astrophysics Supplement, v.117, 393-404. doi: 10.1051/aas:1996164.

Blaauw, R. C., Campbell-Brown, M. D., & Weryk, R. J. (2011), A meteoroid stream survey using the Canadian Meteor Orbit Radar – III. Mass distribution indices of six major meteor showers, Monthly Notices of the Royal Astronomical Society, 414, 3322–3329. https://doi.org/10.1111/j.1365-2966.2011.18633.x.

Bos, B., Jackman, C., & Lauretta, D. S. (2019), Origins, Spectral Interpretation, Resource Identification, Security, Regolith Explorer (OSIRIS-REx): Touch-and-Go Camera Suite (TAGCAMS) Bundle, urn:nasa:pds:orex.tagcams, NASA Planetary Data System.

Bos, B. J., Nelson, D. S., Pelgrift, J. Y., Liounis, A. J., Doelling, D., Norman, C. D., Olds, R. D., … Lauretta, D. S. (submitted), In-flight calibration and performance of the OSIRIS-REx Touch And Go Camera System (TAGCAMS), submitted to Space Science Reviews. doi: 10.1007/s11214-020-00682-x.

Bos, B., Ravine, M. A., Caplinger, M., Schaffner, J. A., Ladewig, J. V., Olds, R. D., … D. S. Lauretta (2018), Touch And Go Camera System (TAGCAMS) for the OSIRIS-REx asteroid sample return mission. Space Sci. Rev. 214, 37. doi:10.1007/s11214-017-0465-2.

Bottke, W. F., Moorhead, A., Connolly, Jr., H. C., Hergenrother, C. W., Molaro, J. L., Michel, P., … Lauretta, D. S. (in review), Meteoroid impacts as a source of Bennu's particle ejection events, JGR Planets.

Bowell, E., Hapke, B., Domingue, D., Lumme, K., Peltoniemi, J., & Harris, A. W. (1989), Application of photometric models to asteroids. In R. P. Binzel, T. Gehrels & M. S. Matthews (Eds.), *Asteroids II* (524-556). Tucson: University of Arizona Press.

Brown, P. G., Hildebrand, A. R., Zolensky, M. E., Grady, M., Clayton, R. N., Mayeda, T. K., … Mazur, T. R. (2000), The fall, recovery, orbit, and composition of the Tagish Lake meteorite: a new type of carbonaceous chondrite, Science, 290, 320-325. doi:10.1126/science.290.5490.320.

Campins, H., Licandro, J., de León, J., Howell, E., Popescu, M., Kaplan, H. H., … Lauretta, D. S. (in review), Asteroid (101955) Bennu in the context of other active asteroids, JGR Planets.

Campins, H., Morbidelli, A., Tsiganis, K., de León, J., Licandro, J., & Lauretta, D. (2010), The origin of asteroid 101955 (1999 RQ36), The Astrophysical Journal Letters, 721, L53. doi:10.1088/2041-8205/721/1/L53.

Chesley, S. R., French, A. S., Davis, A. B., Jacobson, R. A., Brozovic, M., Liounis, A. J., … Lauretta, D. S. (in review), Trajectory estimation for particles observed in the vicinity of (101955) Bennu, JGR Planets.

Chesley, S. R. et al. (2019). Supplementary data for Bennu particle analysis. figshare.com. (Available during review at private URL https://figshare.com/s/19e444f5f6fc9793c919) doi:10.6084/m9.figshare.11328398.

Christensen, E., Africano, B., Farneth, G., Fuls, D., Gibbs, A., Grauer, A., … Shelly, F. (2018), Status of The Catalina Sky Survey for Near Earth Asteroids, American Astronomical Society, DPS meeting #50, id.310.10.

Clark, B. E., Binzel, R. P., Howell, E. S., Cloutis, E. A., Ockert-Bell, A. M., Christensen, P., … Mueller, M. (2011), Asteroid (101955) 1999 RQ36: Spectroscopy from 0.4 to 2.4 μm and meteorite analogs, Icarus, 216, 462-475. doi:10.1016/j.icarus.2011.08.021.

Daly, M.G., Barnouin, O. S., Dickinson, C., Seabrook, J., Johnson, C. L., Cunningham, G., … Lauretta, D. S. (2017), Space Sci. Rev. 212, 899. doi:10.1007/s11214-017-0375-3.

Davidsson, B. J. R., Gutiérrez, P. J., Sierks, H., Barbieri, C., Lamy, P. L., Rodrigo, R., … Vincent, J. -B. (2015), Orbital elements of the material surrounding comet 67P/Churyumov-Gerasimenko, Astro. Astrophys. 583, A16. doi:10.1051/0004-6361/201525841.

Déau, E. (2015), The opposition effect in Saturn's main rings as seen by Cassini ISS: 2. Constraints on the ring particles and their regolith with analytical radiative transfer models, Icarus, 253, 311-345. doi:10.1016/j.icarus.2013.08.031.

Déau, E., Dunes, L., Mishchenko, M. I., West, R. A., Helfenstein, P., Hedman, M. M., & Porco, C. A. (2018), The opposition effect in Saturn's main rings as seen by Cassini ISS: 4. Correlations of the surge morphology with surface albedos and VIMS spectral properties, Icarus, 305, 324-349. doi:10.1016/j.icarus.2017.12.025.

DellaGiustina, D. N., Emery, J. P., Golish, D. R., Rozitis, B., Bennett, C. A., Burke, K. N., … Lauretta, D. S. (2019), Properties of rubble-pile asteroid (101955) Bennu from OSIRIS-REx imaging and thermal analysis. Nat Astron 3, 341–351. doi:10.1038/s41550-019-0731-1.

Fernández, J. A., Licandro, J., Moreno, F., Sosa, A., Cabrera-Lavers, A., de León, J., & Birtwhistle, P. (2017), Physical and dynamical properties of the anomalous comet 249P/LINEAR, Icarus, 295, 34-45. doi:10.1016/j.icarus.2017.04.004.

Fernández, J. A., Sosa, A. (2015), Jupiter family comets in near-Earth orbits: Are some of them interlopers from the asteroid belt?, Planetary and Space Sciences, 118, 14-24. doi:10.1016/j.pss.2015.07.010.

Ferrin, I. (2005), Secular light curve of Comet 28P/Neujmin 1 and of spacecraft target Comets 1P/Halley, 9P/Tempel 1, 19P/Borrelly, 21P/Giacobinni–Zinner, 26P/Grigg–Skjellerup, 67P/Churyumov–Gerasimenko, and 81P/Wild 2, Icarus, 178, 493-516. doi:10.1016/j.icarus.2005.05.007.

Franklin, F. A., & Cook, A. F. (1965), Optical Properties of Saturn's Rings. II. Two-Color Phase Curves of the Two Bright Rings, The Astronomical Journal, 70 (9), 704-720.

Fowler, J. W., & Chillemi, J. R. (1992), IRAS asteroid data processing. In: Tedesco, E.F. (Ed.), The IRAS Minor Planet Survey. Phillips Laboratory, Hanscom Air Force Base, MA, pp. 17–43. Tech. Report PL-TR-92-2049.

Fujiwara, A. (1987), Energy partition into translational and rotational motion of fragments in catastrophic disruption by impact: an experiment and asteroid cases, Icarus, 70, 536-545.

Fujiwara A., & Tsukamoto, A. (1980), Experimental study on the velocity of fragments in collisional breakup, Icarus, 44, 142–153.

Fujiwara, A., & Tsukamoto, A. (1981), Rotation of fragments in catastrophic impact, Icarus, 48, 329-334.

Fuse, T., Yoshida, F., Tholen, D., Ishiguro, M., & Saito, J. (2008), Searching satellites of asteroid Itokawa by imaging observation with Hayabusa spacecraft. Earth Planets Space 60, 33–37. doi:10.1186/BF03352759.

Gault D. E., & Heitowit, E. D. (1963), The partition of energy for hypervelocity impact craters formed in rock, Proc. 6th Hypervelocity Impact Symposium, Vol. 2, pp. 419–456.

Giblin, I., Martelli, G., Farinella, P., Paolicchi, P., Di Martino, M., & Smith, P. N. (1998), The properties of fragments from catastrophic disruption events, Icarus, 134, 77-112.

Green, D. W. E., Marsden, B. G., & Morris, C. S. (2001), Brightness predictions for comets, Astronomy & Geophysics, 42, 1.11-1.12. doi:10.1046/j.1468-4004.2001.0420011.11.x.

Hamilton, V. E., Simon, A. A., Christensen, P. R., Reuter, D. C., Clark, B.E., Barucci, M. A., … Lauretta, D. S. (2019), Evidence for widespread hydrated minerals on asteroid (101955) Bennu. Nat Astron 3, 332–340. doi:10.1038/s41550-019-0722-2.

Hartzell, C. M., Zimmerman, M., Hergenrother, C. W., & Lauretta, D. S. (in review), An evaluation of electrostatic lofting as an active mechanism on Bennu, JGR Planets.

Hergenrother, C. W., Maleszewski, C. K., Nolan, M. C., Li, J. -Y., Drouet d'Aubigny, C. Y., Shelly, F. C., … The OSIRIS-REx Team (2019), The operational environment and rotational acceleration of asteroid (101955) Bennu from OSIRIS-REx observations, Nature Comm. 10, 1291. doi:10.1038/s41467-019-09213-x.

Hergenrother, C. W., Maleszewski, C. K., Chesley, S. R., Li, J. -Y., J. Pelgrift, J. Leonard, J., & Lionius, A. (2019), *Supplemental Data for Bennu Particle Photometry Analysis*. Figshare.com. (Available during review at private URL https://figshare.com/s/08d550cfd745de1a9a60). doi:10.6084/m9.figshare.11573847.

Hergenrother, C. W., Nolan, M. C., Binzel, P. P., Cloutis, E. A., Barucci, M. A., Michel, P., … Lauretta, D. S. (2013), Lightcurve, color and phase function photometry of the OSIRIS-REx target asteroid (101955) Bennu, Icarus, 226, 663-670. doi: 10.1016/j.icarus.2013.05.044.

Hermalyn, B., Farnham, T. L., Collins, S. M., Kelley, M. S., A'Hearn, M. F., & Bodewits, D. (2013), The detection, localization, and dynamics of large icy particles surrounding Comet 103P/Hartley 2, Icarus, 222, 625-633. doi:10.1016/j.icarus.2012.09.030.

Hui, M.-T., & Li, J. (2016), Resurrection of (3200) Phaethon in 2016, Astronomical Journal, 153, 23. doi:10.3847/1538-3881/153/1/23.

Jaumann, R., Schmitz, N., Ho, T. -M., Schröder, S. E., Otto, K. A., Stephan, K., … Kouyama, T. (2019), Images from the surface of asteroid Ryugu shows rocks similar to carbonaceous meteorites, Science, 365(6455), 817-820. doi:10.1126/science.aaw8627.

Jenniskens, P. (2004), 2003 EH1 is the Quadrantid shower parent comet, The Astronomical Journal, 127, 3018-3022. doi:10.1086/383213.

Jewitt, D., Hsieh, H., & Agarwal, J. (2015), The active asteroids, In P. Michel, F. DeMeo & W. Bottke (Eds.), *Asteroids IV* (221-242). Tucson: University of Arizona Press. doi:10.2458/azu_uapress_9780816532131-ch012.

Jewitt, D., & Li, J. (2010), Activity in Geminid parent (3200) Phaethon, Astronomical Journal, 140, 1519. doi:10.1088/0004-6256/140/5/1519.

Kadono, T., Arakawa, M., Ito, T. & Ohtsuki, K. (2009), Spin rates of fast-rotating asteroids and fragments in impact disruption, Icarus, 200, 694-697. doi:1 0.1016/j.icarus.2008.11.021.

Lauretta, D. S., Balram-Knutson, S. S., Beshore, E., Boynton, W. V. Drouet d'Aubigny, C., DellaGiustina, D. N., … Sandford, S. A. (2017), OSIRIS-REx: sample return from asteroid (101955) Bennu, Space Science Reviews 212 (1-2), 925-984. doi:10.1007/s11214-017-0405-1.

Lauretta, D. S., Bartels, A. E. Barucci, M. A. Bierhaus, E. B. Binzel, R. P. Bottke, W. F. … Walsh, K. J. (2015), The OSIRIS-REx target asteroid (101955) Bennu: Constraints on its physical, geological, and dynamical nature from astronomical observations, Meteoritics & Planetary Science, 50 (4), 834-849. doi:10.1111/maps.12353.

Lauretta, D. S., DellaGiustina, D. N., Bennett, C. A. Golish, D. R., Becker, K. J., Balram-Knutson, S. S., … The OSIRIS-REx Team (2019), The unexpected surface of asteroid (101955) Bennu, Nature, 568, 55–60. doi:10.1038/s41586-019-1033-6.

Lauretta, D. S., Hergenrother, C. W. Chesley, S. R., Leonard, J. M., Pelgrift, J. Y., Adam, C. D., … Wolner, C. W. V. (2019), Episodes of particle ejection from the surface of the active asteroid (101955) Bennu, Science, 366, 6470, eaay3544. doi:10.1126/science.aay3544.

Leonard, J. M., Adam, C. D., Pelgrift, J. Y., Lessac-Chenen, E. J., Nelson, D. S., Antreasian, P. G., … Lauretta, D. S. (accepted), Initial Orbit Determination and Event Reconstruction from Estimation of Particle Trajectories about (101955) Bennu, Earth and Space Science.

Levasseur-Regourd, A. -C., Agarwal, J., Cottin, H., Engrand, C., Flynn, G., Fulle, M., …Westphal, A. (2018), Cometary dust, Space Science Reviews, 214 (3), id. 64. doi:10.1007/s11214-018-0496-3.

Licandro, J., Campins, H., Tozzi, G. P., de Leon, J., Pinilla-Alonso, N., Boehnhardt, H., … Hainaut, O. R. (2011). Testing the comet nature of main belt comets. The spectra of 133P/Elst-Pizarro and 176P/LINEAR. Astronomy & Astrophysics, 532, A65. doi: 10.1051/0004-6361/201117018.

Liounis, A. J., Small, J. L., Swenson, J. C., Lyzhoft, J. R., Ashman, B. W., Getzandanner, K. M., … Lauretta, D. S. (in review), Autonomous detection of particles and tracks in optical images, Earth and Space Science.

Kolokolova, L., M. Hanner, M., Levasseur-Regourd, A. -C., & Gustafson, B. A. S. (2004), Physical properties of cometary dust from light scattering and emission, in Comets II, Univ. of Arizona Press, 577-604, 2004.

Kelley, M. S., Linder, D. J., Bodewits, D., A'Hearn, M. F., Lisse, C. M., Kolokolova, L., … Hermalyn, B. (2013), A distribution of large particles in the coma of Comet 103P/Hartley 2, Icarus, 222, 634-652. doi:10.1016/j.icarus.2012.09.037.

Küppers, M., O'Rourke, M. L., Bockelée-Morvan, D., Zakharov, V., Lee, S., von Allmen, P., … Moreno, R. (2014), Localized sources of water vapour on the dwarf planet (1) Ceres. Nature, 505, 525-527. doi: 10.1038/nature12918.

Kwiatkowski, T., Buckley, D., O'Donoghue, D., Crause, L., Crawford, S., Hashimoto, Y., … Sefako, R. (2010), Photometric survey of the very small near-Earth asteroids with the SALT telescope I. Lightcurves and periods for 14 objects. Astronomy & Astrophysics, 509, A94. doi:10.1051/0004-6361/200913152.

Macke, R. J., Consolmagno, G. J., & Britt, D. T. (2011), Density, porosity, and magnetic susceptibility of carbonaceous chondrites, Meteoritics and Planetary Sciences, 46, 1842-1862. doi:10.1111/j.1945-5100.2011.01298.x.

Marchi, S., Chapman, C. R., Barnouin, O. S., Richardson, J. E., & Vincent, J. -B. (2015), Cratering on Asteroids, In Patrick Michel, Francesca E. DeMeo, and William F. Bottke (Eds.), *Asteroids IV* (725-744). Tucson, University of Arizona Press. doi:10.2458/azu_uapress_9780816532131-ch037.

McFadden, L. A., Skillman, D. R., Memarsadeghia, N., Carsenty, U., Schröder, S. E., Li, J. -Y., … Russell, C. T. (2018), Vesta's missing moons: comprehensive search for natural satellites of Vesta by the Dawn spacecraft, Icarus, 257, 207–216. doi:10.1016/j.icarus.2018.02.017.

McFadden, L. A., Skillman, D. R., Memarsadeghia, N., Li, J. -Y., Joy, S. P., Polanskey, C. A., … Russell, C. T. (2015), Vesta's missing moons: comprehensive search for natural satellites of Vesta by the Dawn spacecraft. Icarus, 257, 207–216. doi:10.1016/j.icarus.2015.04.038.

Michikami, T., Hagermann, A., Kadokawa, T., Yoshida, A., Shimada, A., Hasegawa, S., & Tsuchiyama, A. (2016). Fragment shapes in impact experiments ranging from cratering to catastrophic disruption, Icarus, 264, 316-330. doi:1301/10.1016/j.icarus.2015.09.038.

Mink, D. J. (1997), WCSTools: putting image world coordinate systems to use, in Astronomical Data Analysis Software and Systems VI, A.S.P. Conference Series, Vol. 125. Edited by Gareth Hunt and H. E. Payne. San Francisco: Astronomical Society of the Pacific, pp. 249-252.

Moffat, A. F. J. (1969), A theoretical investigation of focal stellar images in the photographic emulsion and application to photographic photometry, Astronomy and Astrophysics, 3, 455.

Molaro, J. L., Hergenrother, C. W., Chesley, S. R., Hanna, R. D., Haberle, C. W., Ballouz, R. -L., … Lauretta, D. S. (in review), Thermal fatigue as a driving mechanism for activity on asteroid Bennu, JGR Planets.

Muinonen, K., Belskaya, I. N., Cellino, A., Delbó, M., Levasseur-Regourd, A. -C., Penttilä, A. & Tedesco, E. F. (2010), A three-parameter magnitude phase function for asteroids, Icarus, 209, 542–555. doi:10.1016/j.icarus.2010.04.003.

Muñoz, O., Moreno, F., Guirado, D., Dabrowska, D. D., Volten, H., & Hovenier, J. W. (2012), The Amsterdam-Granada light scattering database, Journal of Quantitative Spectroscopy and Radiative Transfer, 113, 565-574. doi:10.1016/j.jqsrt.2012.01.014.

Muñoz, O., Moreno, F., Vargas-Martín, F., Guirado, D., Escobar-Cerezo, J., Min, M., & Hovenier, J. W. (2017), Experimental phase functions of millimeter-sized cosmic dust grains, Astronomical Journal, 846, 1. doi:10.3847/1538-4357/aa7ff2.

Pajola M., Lucchetti, A., Fulle, M., Mottola, S., Hamm, M., Da Deppo, V., … Thomas, N. (2017), The pebbles/boulders size distributions on Sais: Rosetta's final landing site on comet 67P/Churyumov-Gerasimenko, MNRAS, 469, S636-S645. doi:10.1093/mnras/stx1620.

Pelgrift, J. Y., Lessac-Chenen, E. J., Adam, C. D., Leonard, J. M., Nelson, D. S., McCarthy, L., … Lauretta, D. S. (accepted), Reconstruction of Bennu particle events from sparse data, Earth and Space Science.

Poulet, F., Cuzzi, J. N., French, R. G., & Dones, L. (2002), A Study of Saturn's Ring Phase Curves from HST Observations, Icarus, 158, 224-248. doi:10.1006/icar.2002.6852.

Pravec, P., & Harris, A. W. (2007), Binary asteroid population: 1. Angular momentum content, Icarus, 190(1), 250-259. doi:10.1016/j.icarus.2007.02.023.

Pravec, P., Hergenrother, C., Whiteley, R., Sarounova, L., Kusnirak, P., & Wolf, M. (2000), Fast Rotating Asteroids 1999 TY2, 1999 SF10, and 1998 WB2, Icarus, 147, 477-486. doi: 10.1006/icar.2000.6458.

Rozitis, B., Emery, J. P.,Siegler, M. A., Susorney, H. C. M., Molaro, J. L., Hergenrother, C. W., & Lauretta, D. S. (accepted), Implications for ice stability and particle ejection from high-resolution temperature modeling of asteroid (101955) Bennu, JGR Planets.

Samarasinha, N. H., & Larson, S. M. (2014), Image enhancement techniques for quantitative investigations of morphological features in cometary comae: a comparative study, Icarus, 239, 168-185. doi: 10.1016/j.icarus.2014.05.028.

Scheeres, D. J., McMahon, J. W., French, A. S., Brack, D. N., Chesley, S. R., Farnocchia, D., … Lauretta, D. S. (2019), The dynamic geophysical environment of (101955) Bennu based on OSIRIS-REx measurements. Nat Astron 3, 352–361. doi:10.1038/s41550-019-0721-3.

Shevchenko, V.G., Chiorny, V. G., Gaftonyuk, N. M., Krugly, Y. N., Belskaya, I. N., Tereschenko, I. A., & Velichko, F. P. (2008), Asteroid observations at low phase

angles. III. Brightness behavior of dark asteroids, Icarus, 196, 601–611. doi:10.1016/j.icarus.2008.03.015.

Stetson, P. B. (1987), DAOPHOT: A computer program for crowded-field stellar photometry, PASP, 99, 191-222. doi:10.1086/131977.

Taylor, P. A., Rivera-Valentín, L. E. G., Benner, L. A. M., Marshall, S. E., Virkki, A. K., Venditti, F. C. F., … Giorgini, J. G. (2019), Arecibo radar observations of near-Earth asteroid (3200) Phaethon during the 2017 apparition, Planetary and Space Sciences, 167, 1-8. doi:10.1016/j.pss.2019.01.009.

Veres, P., Jedicke, R., Denneau, L., & Wainscoat, R. (2012), Improved asteroid astrometry and photometry with trail fitting, PASP, 124, 1197-1207. doi:10.1086/668616.

Vincent, J.-B., Farnham, T., Kührt, E., Skorov, Y., Marschall, R., Oklay, N., … Keller, H. U. (2019), Local manifestations of cometary activity, Space Sci. Rev., 215, 30. doi:10.1007/s11214-019-0596-8.

Watanabe, S., Hirabayashi, M., Hirata, N., Hirata, Na., Noguchi, R., Shimaki, Y., … Tsuda, Y. (2019), Hayabusa2 arrives at the carbonaceous asteroid 162173 Ryugu—A spinning top–shaped rubble pile, Science, 364, 268-272. doi: 10.1126/science.aav8032.

Watson, E., Gulde, M., Kortmann, L., Higashide, M., Schaefer, F., & Hiermaier, S. (2019), Optical fragment tracking in hypervelocity impact experiments, Acta Astronautica, 155, 111-117. doi:10.1016/j.actaastro.2018.11.036.

Waza, T., & Matsui, T. (1985), Laboratory simulation of planetesimal collision 2. Ejecta velocity distribution, Journal of Geophysical Research, 90 1995-2011.

Whipple, F. L. (1983), 1983 TB and the Geminid meteors, eds. B. G. Marsden, IAU Circular 3881.

Ye, Q. (2019), Prediction of meteor activities from (101955) Bennu, Res. Notes AAS, 3, 56. doi:10.3847/2515-5172/ab12e7.

Zacharias, N., Finch, C. T., Girard, T. M., Henden, A., Bartlett, J. L., Monet, D. G., & Zacharias, M. I. (2013), The Fourth US Naval Observatory CCD Astrograph Catalog (UCAC4), The Astronomical Journal, 145(2), id. 44. doi:10.1088/0004-6256/145/2/44.

Zappala, V., Cellino, A., Barucci, A. M., Fulchignoni, M., & Lupishko, D. F. (1990), An analysis of the amplitude-phase relationship among asteroids, Astronomy & Astrophysics, 231, 548-560.